Pergamon

Planet. Space Sci., Vol. 46, No. 1, pp. 1–20, 1998

0032-0633/98 $19.00+0.00

PII: S0032-0633(97)00126-8

Voyager 2 ultraviolet spectrometer solar occultations at Neptune: photochemical modeling of the 125–165 nm lightcurves

James Bishop,[1] Paul N. Romani[2] and Sushil K. Atreya[3]

[1]Computational Physics, Inc., 2750 Prosperity Avenue, Suite 600, Fairfax, VA 22031, U.S.A.
[2]Code 693.2, NASA/Goddard Space Flight Center, Greenbelt, MD 20771, U.S.A.
[3]Department of Atmospheric, Oceanic and Space Sciences, University of Michigan, Ann Arbor, MI 48109, U.S.A.

Received 1 November 1996; accepted 24 May 1997

Abstract. Abstract. Ingress and egress Voyager 2 ultraviolet spectrometer (UVS) solar occultation lightcurves at wavelengths longward of HI Lyman α acquired during the Neptune encounter are compared with one-dimensional methane photochemical–transport models to infer hydrocarbon abundances and the strength of eddy mixing in the stratosphere. Previous modeling of the 125–140 nm lightcurves indicated eddy mixing coefficient (K) values of $3–10\times10^6\,cm^2\,s^{-1}$ near the 0.2 μbar level and methane mixing ratios in the lower stratosphere on the order of $1–3\times10^{-4}$; these results should be insensitive to photochemical details, provided methane is the main source of opacity at these wavelengths. The UVS lightcurves at the longer wavelengths, which probe beneath the CH_4 photolysis peak, are expected to be dominated by the opacity of C_2 species (ethane, acetylene, ethylene) and perhaps higher order organics. At wavelengths >152 nm, H_2 Rayleigh scattering is also a major opacity source. Modeled C_2 species abundances are sensitive to modeling details, especially the strength and height profile of eddy mixing. The current photochemical model incorporates several updates, including a recent revision in CH_4 photolysis branching ratios at Lyman α. In the photochemical modeling reported here, various forms for the eddy mixing profile have been tested, with the constraint that the models for egress conditions remain consistent with the C_2H_6 and C_2H_2 abundances near 0.5 mbar derived from IRIS measurements. Superior fits are obtained with models exhibiting a stagnant lower stratosphere ($K\approx2\times10^3\,cm^2\,s^{-1}$ for pressures >2 mbar) with a rapid transition to a localized level of vigorous eddy mixing in the upper stratosphere ($K\approx10^8\,cm^2\,s^{-1}$ near 10 μbar, decreasing at higher altitudes). In line with our earlier work, methane mixing ratios on the order of 10^{-4} are required to obtain good agreement between the photochemical models and the UVS lightcurves.

1. Introduction

During the Voyager 2 flyby of Neptune, both ingress and egress solar occultations were recorded with the ultraviolet spectrometer (UVS) instrument (Broadfoot *et al.*, 1989). The transmission profiles or lightcurves defined by the progressive absorption with decreasing minimum tangent ray height (MTRH) of the solar irradiance within each UVS channel probed the Neptune atmosphere at two latitudes (61°N near the winter hemisphere arctic circle, 49°S in the summer hemisphere at the time of encounter). At wavelengths longward of H Lyman α (121.6 nm), the lightcurves penetrated to stratospheric levels (0.1 μbar $> p >$ 0.1 mbar). In a previous paper (Bishop *et al.*, 1992, hereafter referred to as Paper 1), we presented a modeling analysis of the UVS lightcurves at wavelengths of 125–140 nm using a one-dimensional steady-state methane photochemical–transport code, based on the expectations that methane (CH_4) and its photochemical progeny were the species responsible for the measured opacity and that the source of methane in the stratosphere was upward transport from deeper levels. The main results were estimates of the strength of eddy mixing in the vicinity of the half-light altitudes of the 125–140 nm lightcurves ($K_{1/2}\approx3–10\times10^6\,cm^2\,s^{-1}$ at 550–600 km above the 1 bar levels) and compatible methane mixing ratios in the lower stratosphere ($f_T(CH_4)\approx1–3\times10^{-4}$). In this report, we discuss our attempts to model the occultation data at wavelengths 140–165 nm. These data probe the stratosphere at altitudes beneath the primary photochemical zone (identified by the level at which unit optical depth for Lyman α absorption by methane occurs). As a consequence, it is

Correspondence to: James Bishop

possible to use these data in conjunction with Voyager measurements pertaining to deeper pressure levels to constrain models for the eddy mixing coefficient throughout the stratosphere.

The photochemical model has been updated since Paper 1. More recently, it has been used in a combined study of Voyager measurements at Neptune on stratospheric hazes and hydrocarbon species (Romani *et al.*, 1993, hereafter referred to as Paper 2). Even though Paper 2 was not concerned with detailed modeling of the UVS lightcurves, comparisons of the various model cases with the UVS egress occultation data were presented to illustrate the impact on modeling results of the adoption of different eddy mixing and atmospheric temperature height profiles; alternate low-temperature rate coefficients for several key reactions were also tested. The form adopted for the height variation of the eddy mixing coefficient is of crucial importance. The form introduced in Paper 2 characterizing the most successful models derived from preliminary explorations in modeling the longer wavelength UVS lightcurves. While a variety of different K profiles have been explored, the form illustrated by Models B, C, and D of Paper 2, with a localized zone of rapid mixing overlying a stagnant lower stratosphere, has proven to be the most successful at replicating the UVS lightcurves while, in the egress case, remaining consistent with the IRIS measurements analyzed by Bézard *et al.* (1991).

In the following sections, the UVS lightcurves used in our modeling are presented and the simulation procedure is described, including a complete listing of modeling inputs and chemical reaction rates. Photochemical models and data–model lightcurve comparisons are then presented and discussed.

2. UVS lightcurves

Our handling of the UVS data is described in Paper 1, although for the current modeling we have decided not to rescale the data. In Fig. 1, a subset of the UVS solar occultation data used in our modeling is shown as transmission lightcurves ($I(z_\perp,\lambda_c)/I_o(\lambda_c)$, where $z_\perp$ is the minimum tangent ray height) averaged over 0.96 s intervals and ordered according to the channel center wavelengths λ_c at 500 km MTRH. Altitude resolutions, defined by the change in MTRH over a data-accumulation interval, are 9.6 km (ingress) and 12.3 km (egress), and the spectral resolution is 2.5 nm. The apparent solar diameter for both occultations (4 km at ingress, 20 km at egress) is small relative to the MTRH range over which total opacities drop from 0.9 to 0.1 and has been ignored. Other aspects of the occultation (e.g., channel center offsets as functions of MTRH stemming from the limit cycle motion, convolution of model transmission spectra at 0.1 nm resolution with the UVS slit function) are incorporated in our modeling using the information provided to us by B. Sandel and R. Vervack (personal communication).

In addition to measurement noise, the data are afflicted by two main sources of error: internal instrument scattering, primarily of the solar Lyman α line, and pointing uncertainties which introduce uncertainties in the ratioing. These errors and the derivation of a corresponding standard deviation σ_D are discussed by Yelle *et al.* (1993). In recognition of this, we display the UVS data as data ranges defined by $I(z_\perp,\lambda_c)/I_o(\lambda_c)\pm\sigma_D$ when making comparisons with model lightcurves.

3. Modeling procedure

The model lightcurves are constructed using the H_2 density distributions provided by the model atmospheres and the hydrocarbon (CH_4, C_2H_2, C_2H_4, C_2H_6) density distributions obtained from solving the coupled 1-D continuity equations

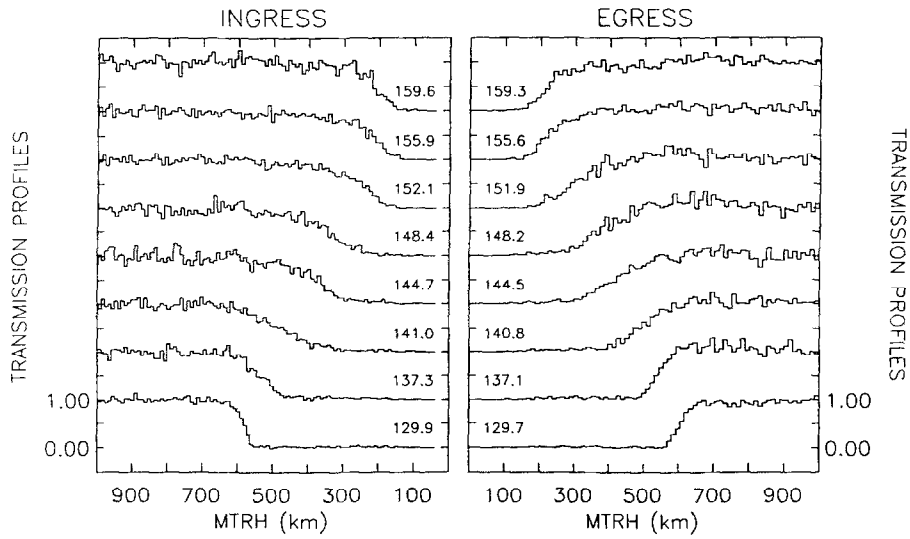

Fig. 1. Single channel ingress and egress UVS solar occultation lightcurves at wavelengths 130–160 nm, labeled by channel center wavelength at 500 km minimum tangent ray height (MTRH). The time series of I/I_o measurements recorded by the UVS instrument have been binned over 0.96 s intervals, resulting in a nominal MTRH resolution of 9.6 km for the ingress occultation and 12.3 km for the egress occultation. MTRH are referenced to the respective 1 bar radii: 24445 km for ingress and 24535 km for egress (Lindal, 1992)

Table 1. Variable definitions

Symbol	Definition
f_i, n_i	mixing ratio, number density (molecules cm^{-3}) of species i
Φ_i	net vertical flux of species i (molecules $cm^{-2}s^{-1}$)
P_i	chemical production rate of species i (molecules $cm^{-3}s^{-1}$)
L_i	chemical loss rate of species i (molecules $cm^{-3}s^{-1}$)
D_i	molecular diffusion coefficient of species i for the background H_2–He atmosphere (cm^2s^{-1})
K	atmospheric eddy mixing coefficient (cm^2s^{-1})
n	atmospheric number density (molecules cm^{-3})
p	atmospheric pressure (mbar)
T	atmospheric temperature (K)
z, r	altitude, radial distance from center of planet (cm, km)
H_i	partial pressure scale height of species i (cm)
H_{atm}	atmospheric pressure scale height (cm)
h_i	local density scale height of species i (cm)
h_{atm}	local atmospheric density scale height (cm)
λ	wavelength (nm, Å)
λ_c	channel center wavelength at $z_\perp$ (nm, Å)
$\Delta_s\lambda$	UVS channel spectral width (nm, Å)
$R(\lambda-\lambda_c)$	normalized instrument response at λ in channel with center wavelength λ_c
I_o	reference solar flux at top of atmosphere (photons $cm^{-2}s^{-1}Å^{-1}$)
σ_i	photoabsorption cross section of species i (cm^2 molecule^{-1})
$z_\perp$, $r_\perp$	minimum tangent ray height, radial distance for line of sight to center of solar disk (cm)
$z_{1/2}$	tangent altitude above 1 bar level where $I/I_o = 1/2$ for the $\lambda_c < 140$ nm channels (cm, km)
$I(z_\perp,\lambda_c)$	measured solar irradiance at $z_\perp$ in channel with center wavelength λ_c
$I_o(\lambda_c)$	measured solar irradiance in channel with center wavelength λ_c without attenuation
σ_D	effective standard deviation in measured transmission profile $I(z_\perp,\lambda_c)/I_o(\lambda_c)$
$f_T(CH_4)$	lower stratospheric methane mixing ratio
$K_{1/2}(\lambda_c)$	eddy mixing coefficient at the half-light point of channel λ_c (cm^2s^{-1})
$\phi^T(H)$	atomic hydrogen flux at upper boundary (atoms $cm^{-2}s^{-1}$)
w_D	diffusive speed (molecular diffusion) ($cm\,s^{-1}$)
τ_K	eddy mixing transport timescale (s)
τ_D	molecular diffusion transport timescale (s)
$\tau_{production}$	photochemical production timescale (s)
τ_{loss}	photochemical loss timescale (s)

$$\frac{d\Phi_i}{dz} = P_i - L_i \qquad (1)$$

for each species i assuming steady-state conditions. (Variables are defined in Table 1.) In terms of the mixing ratio for species i, the flux is (ignoring the small thermal diffusion term)

$$\Phi_i = -n\left[(D_i+K)\frac{df_i}{dz} + D_i f_i(H_i^{-1} - H_{atm}^{-1})\right]. \qquad (2)$$

Once the hydrocarbon abundances are evaluated, simulated UVS lightcurves are given by

$$\bar{I}(r_\perp,\lambda_c) = \int_{\lambda_c-\Delta_s\lambda}^{\lambda_c+\Delta_s\lambda} R(\lambda-\lambda_c)I_o(\lambda)$$
$$\exp\left[-2\int_{r_\perp}^{\infty} dr \frac{r}{(r^2-r_\perp^2)^{1/2}} n(z)\sum_i f_i(z)\sigma_i(\lambda)\right] d\lambda. \qquad (3)$$

The species included in the model undergoing photochemical production, loss, and transport are CH_4, CH_3, $^3CH_2$, C_2H_2, C_2H_3, C_2H_4, C_2H_5, C_2H_6, C_4H_2, and atomic hydrogen. The following species are treated as being in local chemical equilibrium: CH, $^1CH_2$, C_2, C_2H, CH_3C_2H, C_4H, $C_4H_2^*$, and C_4H_3. Fixed-point (mixing ratio) boundary conditions are used for all transported species at the lower boundary (the tropopause); at the upper boundary ($p = 10^{-5}$ mbar), flux values are specified. For the hydrocarbon species, the upper boundary fluxes are all set to zero; the nominal magnitude adopted for the downward flux of atomic hydrogen from thermospheric EUV-driven processes is $4\times10^7\,cm^{-2}s^{-1}$, adapted from Gladstone (1983).

The main fitting parameters are the mixing ratio of methane in the lower stratosphere ($f_T(CH_4)$) and the parameters defining the eddy mixing coefficient (K) profile. We have explored several different profile forms for K. In seeking out successful model fits, our first step is to identify [$f_T(CH_4)$, $K_{1/2}(\lambda_c < 140\,nm)$] pairs providing the best agreement with the UVS data at wavelengths shortwards of 140 nm (i.e. the procedure of Paper 1). As previously noted, these lightcurves are expected to be least sensitive to photochemical modeling details. The K profile is then systematically varied, as allowed by the adopted form while maintaining the fit at wavelengths < 140 nm, to try to improve the fit of the model transmission profiles to the UVS data at longer wavelengths. As in Paper 1, we rely on visual judgements in assessing the quality of model agreement with the data. The nominal values derived for the fitting parameters are not unique and can be modified by perhaps 50% without adversely affecting the data–model comparisons, provided the modifications compensate one another (e.g. an increase in $f_T(CH_4)$ requires a compensating decrease in $K_{1/2}(\lambda_c < 140\,nm)$ in order to maintain the correct placement ($z_{1/2}$) of the $\lambda_c < 140$ nm half-light levels.)

The analysis by Bézard *et al.* (1991) of IRIS measurements of stratospheric hydrocarbon emissions obtained during the Neptune flyby is based on a large selection of low spatial resolution data with field-of-view centers ranging from 10°S to 50°S latitude, which contains the UVS egress occultation latitude. Consequently, the acetylene and ethane mixing ratios (4×10^{-8} (0.2 mbar) and 1.3×10^{-6} (0.7 mbar), respectively) derived by Bézard *et al.* have been adopted as important constraints for our photochemical models in the egress case.

4. Modeling inputs

4.1. *Atmosphere model*

The atmospheric mean molecular weight adopted in our modeling is 2.393, with a helium mixing ratio f(He) of

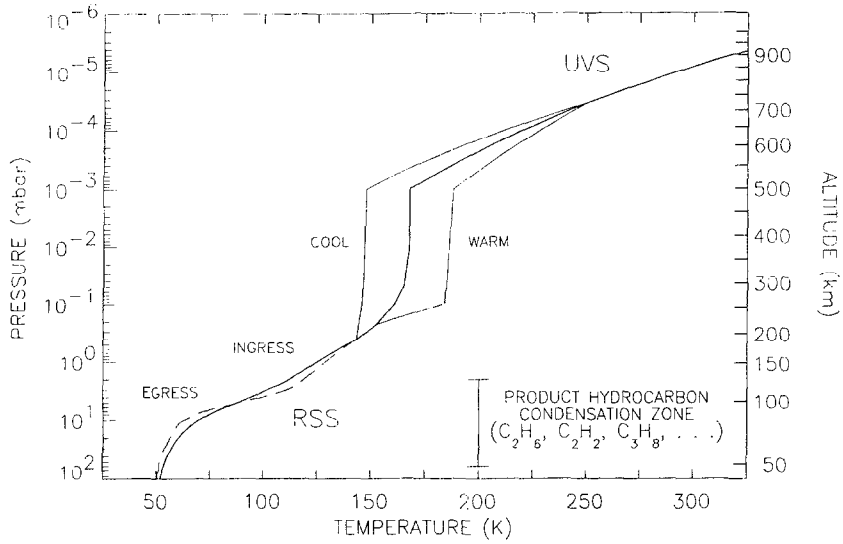

Fig. 2. Ingress and egress p–T models (see text). The altitude scale for the nominal ingress p–T model is shown on the right hand ordinate axis. The region where photochemically produced hydrocarbons are predicted to condense is also indicated (Moses *et al.*, 1992; Romani *et al.*, 1993)

0.19 (Conrath *et al.*, 1991a): the possibility that $f(\mathrm{He}) = 0.15$ with $f(\mathrm{N_2}) \approx 0.003$ (Conrath *et al.*, 1993) does not impact the modeling results presented in Section 5. Atmospheric pressure–temperature (p–T) profiles at pressures deeper than ≈ 2 mbar at the ingress and mean egress latitudes are taken from the RSS occultations analysis of Lindal (1992). These are extended to 1.0 μbar using a profile of the form presented by Hubbard *et al.* (1987); after scaling to $f(\mathrm{He}) = 0.19$, their analysis of the 20 August 1985 stellar occultation central flash indicates a temperature of 143 K near 0.42 mbar. The nominal 1 μbar temperature is 168 K, taken from Orton *et al.* (1992). The high altitude segment is based on the preliminary analysis of the UVS ingress solar occultation data presented by Broadfoot *et al.* (1989). The composite profile is shown in Fig. 2. The 1 bar radii at the UVS occultation latitudes, which are needed to place the p–T profiles on an altitude scale, are taken from Lindal (1992): 24445 km at the ingress latitude of 61° N and 24535 km at the mean egress latitude of 49° S.

Since the p–T profile is not well-constrained by Voyager flyby data at pressures in the range 2 mbar to 0.01 μbar, "warm" and "cool" models have been used in the modeling. These are defined by shifting the 1 μbar temperature of Orton *et al.* (1992) by ± 20 K as suggested by numerous stellar occultations (Roques *et al.*, 1994). In these models, the RSS profiles and the Hubbard *et al.* 0.42 mbar point are not modified.

4.2. *Solar irradiance spectrum*

Photolysis rates are calculated using solar irradiance fluxes summed over 10 Å intervals spanning the wavelength range 1000–2500 Å. At wavelengths longward of 1204 Å, the fluxes are from the 1985 Spacelab-2 flight of SUSIM (VanHoosier *et al.*, 1988); a scaled ($F_{10.7} = 207$) Hinteregger spectrum is used at shorter wavelengths (Hinteregger *et al.*, 1981). The composite spectrum at 1 AU is shown in Fig. 3 and is representative of solar near-maximum conditions; the line-integrated Lyman α flux is 6.5×10^{11} ph cm^{-2} s^{-1}. (Note that although the SUSIM spectrum was obtained near solar minimum, the Lyman α flux value is relatively large. It is unfortunate that no FUV solar spectral irradiance measurements of comparable spectral resolution are available for the period of the Neptune encounter.) At Neptune's distance from the Sun, the pervasive Lyman α skyglow associated with the local interstellar medium (LISM) is not negligible and has been included in the modeling; near-encounter measurements by the Voyager UVS give an estimate of 420 R for the sky-averaged LISM Lyman α brightness, giving a contribution to the CH_4 photolysis rate of 4×10^{-9} s^{-1} at the top of the atmosphere. By comparison, the photolysis rate driven by the direct SUSIM solar flux is 1.3×10^{-8} s^{-1}. The SUSIM spectrum at 1 Å resolution is also employed in the lightcurve simulations.

In our modeling, we adopt "local" conditions, i.e. model atmospheres and photolysis rates corresponding to conditions at the occultation latitudes at the time of encounter. Our modeling of the UVS lightcurves suggests rapid eddy mixing at pressures 1 μbar $< p <$ 0.1 mbar, so that the timescale for mixing ($\tau_K = h_{\mathrm{atm}}^2/K$) is significantly shorter than a solar cycle (and consequently much shorter than a Neptune season). The analysis of the UVS data by Yelle *et al.* (1993) suggests $K \approx 10^5$ cm^2 s^{-1}, which is smaller than the magnitude we infer at the same pressures; even with this value, though, the mixing timescales are significantly shorter than seasonal or solar cycle timescales. The effective solar zenith angles adopted in the ingress and egress modeling are 89.2° and 40.2°, respectively, corresponding to diurnally averaged solar illumination conditions at the time of encounter.

4.3. *Photoabsorption cross sections*

The photoabsorption cross sections used in the opacity modeling are shown in Fig. 4, at roughly 2 Å resolution.

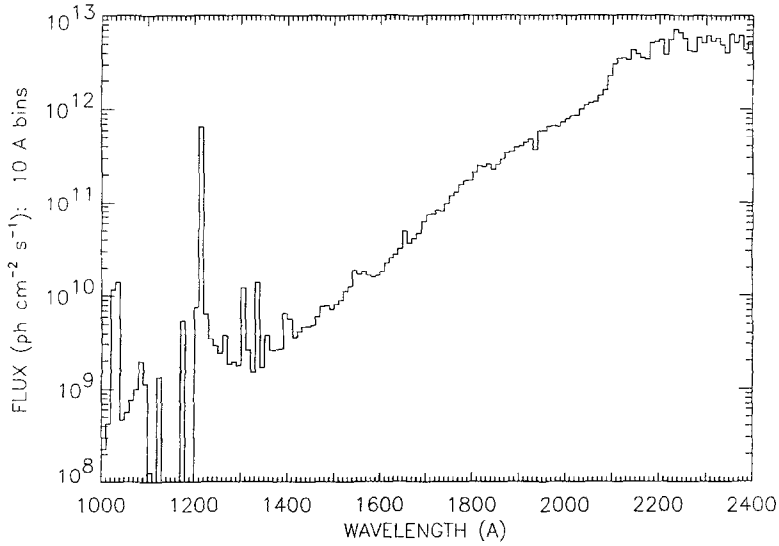

Fig. 3. Solar FUV irradiance spectrum at 1 AU adopted in the photochemical modeling and lightcurve simulations. The Lyman α flux is 6.5×10^{11} photons cm^{-2} s^{-1}. (See text.)

These are taken from:

CH_4	Lee and Chiang (1983); Mount *et al.* (1977)
C_2H_2	Suto and Lee (1984); Wu *et al.* (1989); R. Wu, personal communication ($T = 155$ K)
C_2H_4	R. Wu, personal communication ($T = 155$ K)
C_2H_6	Mount and Moos (1978)
C_4H_2	Glicker and Okabe (1987)

Superimposed are the cross sections convolved with the UVS instrument slit function. The channel center wavelengths for the ingress occultation data at a tangent altitude of 500 km are also indicated.

The photolysis channels and branching ratios included in the photochemical modeling are listed in Table 2. The recent revision in the direct quantum yield of CH_3 from the photolysis of methane at Lyman α (Mordaunt *et al.*, 1993) has been folded into our modeling. However, since the story of CH_4 Lyman α photolysis is still incomplete,

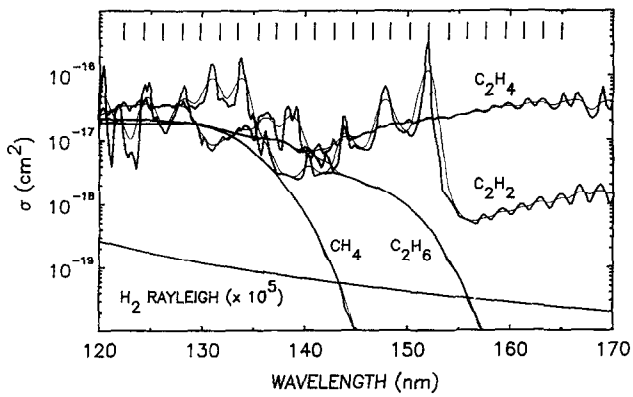

Fig. 4. UV photoabsorption cross sections for CH_4, C_2H_2, C_2H_4, and C_2H_6, at a spectral resolution of ~0.2 nm (see text). The lighter weight lines show the photoabsorption spectra degraded with the nominal UVS slit function. Also shown are the H_2 Rayleigh–Raman scattering cross sections taken from Ford and Browne (1973), scaled upward by a factor 10^5. The hash marks along the top of the figure indicate the UVS channel center wavelengths at 500 km MTRH (ingress occultation)

we have attempted to make reasonable estimates of the branching ratios for each energy-allowed channel. These estimates are discussed in detail in Appendix A.

4.4. *Chemical reaction rates*

The chemical reactions included in the modeling are listed in Table 3 along with the adopted rates. There have been several updates to the modeled chemistry since the study presented in Paper 2. The most notable changes are (1) the introduction of the photolysis channel $CH_4 + h\nu \rightarrow CH_3 + H$ using the results of Mordaunt *et al.* (1993) and (2) revision of the chemical pathways involving the vinyl radical (C_2H_3) (Romani, 1996). The chemical scheme is fairly complete for the C_2 hydrocarbons. An expanded chemical scheme with a more complete coverage of reaction paths involving C_3 and C_4 species was used by Moses *et al.* (1992) in their pre-encounter study of hydrocarbon photochemistry and condensation in Neptune's stratosphere. (A comparative discussion of the Romani *et al.* (1993) and Moses *et al.* (1992) studies is given in Bishop *et al.* (1995).)

4.5. *Condensation*

In the lower stratosphere, temperatures are cold enough to result in very high supersaturations (S) for several hydrocarbon species (principally C_2H_6 and C_2H_2) if these remained in the gas phase. Consequently, a condensation loss is included. Our handling of this loss mechanism is discussed in detail in Paper 2; the nominal placement for removal from the gas phase is dictated by the condition $S \geq 1$. The study of the relative efficiency of condensation processes by Moses *et al.* (1992) suggests that the condensation levels of product hydrocarbons should lie deeper in the atmosphere than indicated by the $S \geq 1$ condition; however, both the IRIS and UVS hydrocarbon data refer to pressure levels ($p \approx 0.5$ mbar and

Table 2. Photolysis channels and references

		Reaction	Branching ratios[a]	References
J1[b]	$CH_4+h\nu$	$\xrightarrow{a} {}^3CH_2+H+H$ $\xrightarrow{b} {}^1CH_2+H_2$ $\xrightarrow{c} CH+H+H_2$ $\xrightarrow{d} CH_3+H$ $\xrightarrow{e} {}^1CH_2+H+H$	$q_a(121.6)=0.212$ $q_b(121.6)=0.282$ $q_c(121.6)=0.100$ $q_d(121.6)=0.406$ $q_e(121.6)=0.0$	Lee and Chiang (1983); Mount *et al.* (1977); McNesby and Okabe (1964); Calvert and Pitts (1966); Rebbert and Ausloos (1972); Gorden and Ausloos (1967); Slanger and Black (1982); Mordaunt *et al.* (1993); Laufer and McNesby (1968)
J2	$C_2H_2+h\nu$	$\xrightarrow{a} C_2H+H$	$q_a(\lambda<153)=0.30$ $q_a(153<\lambda<186)=0.12$ $q_a(186<\lambda<201)=0.21$	Okabe (1981); Okabe (1983); Shin and Michael (1991); McDonald *et al.* (1978); Suto and Lee (1984); Wu *et al.* (1989); Nakayama and Watanabe (1964); R. Wu, personal communication, 1991
		$\xrightarrow{b} C_2+H_2$	$q_b(\lambda<201)=0.10$	
J3	$C_2H_4+h\nu$	$\xrightarrow{a} C_2H_2+H_2$ $\xrightarrow{b} C_2H_2+H+H$	$q_a(\lambda<190)=0.51$ $q_b(\lambda<190)=0.49$	Xia *et al.* (1991); R. Wu, personal communication, 1991; Hara and Tanaka (1973); Sauer and Dorfman (1961); Back and Griffiths (1967)
J4	$C_2H_6+h\nu$	$\xrightarrow{a} C_2H_2+H_2+H_2$	$q_a(121.6)=0.25$ $q_a(\lambda<170)=0.27$	Mount and Moos (1978); Calvert and Pitts (1966); Akimoto *et al.* (1965); Lias *et al.* (1970); Hampson and McNesby (1965)
		$\xrightarrow{b} C_2H_4+H+H$	$q_b(121.6)=0.30$ $q_b(\lambda<170)=0.14$	
		$\xrightarrow{c} CH_4+{}^1CH$	$q_c(121.6)=0.25$ $q_c(\lambda<170)=0.02$	
		$\xrightarrow{d} C_2H_4+H_2$	$q_d(121.6)=0.13$ $q_d(\lambda<170)=0.56$	
		$\xrightarrow{e} C_2H_4+H_2CH_3+CH_3$	$q_e(121.6)=0.08$ $q_e([\lambda<170)=0.01$	
J5	$C_4H_2+h\nu$	$\xrightarrow{a} C_4H+H$	$q_a(\lambda<166)=0.20$	Okabe (1981); Glicker and Okabe (1987); Allan (1984)
		$\xrightarrow{b} C_2H_2+C_2$	$q_b(\lambda<166)=0.10$ $q_b(166<\lambda<207)=0.06$	
		$\xrightarrow{c} C_2H+C_2H$	$q_c(\lambda<166)=0.03$ $q_c(166<\lambda<207)=0.01$	
		$\xrightarrow{d} C_4H^{**}{}_2$	$q_d(\lambda<166)=0.67$ $q_d(166<\lambda<207)=0.93$ $q_d(\lambda>207)=1.00$	
J6[c]	$C_4H^*_2$	$\xrightarrow{a} C_4H_2+h\nu$	$A_d=1000.0\,s^{-1}$	assumed
J7	$CH_3+h\nu$	$\xrightarrow{a} {}^1CH_2+H$	$q_a(\lambda=216.4)=1.00$	Arthur (1986)

[a] Wavelengths in nm.
[b] See text.
[c] Assuming the radiative lifetime of $C_4H^*_2$ to be 10^{-3} s.

$p<0.1$ mbar, respectively) well above the condensation levels so that modeling of these data are only indirectly affected by the exact placement of these levels. Within the context of the current study, the significance of condensation is in establishing an efficient loss mechanism acting at a deeper level resulting in downward fluxes of acetylene and ethane throughout the pressure regions sounded by the IRIS and UVS data.

5. Data–model comparisons

K profiles of the form

$$K(z)=K_o\left(\frac{n_o}{n(z)}\right)^{\beta} \tag{4}$$

with $\beta=0.5$ (the subscript o refers to a reference level) have been used in generating the model results shown Fig. 5, since this type of profile (Lindzen, 1971; Hunten, 1975) has been commonly used in photochemical modeling studies of outer planet stratospheres. The fits are determined by the $\lambda_c<140$ nm channels, and it is apparent that the C_2 hydrocarbon abundances in these models are not consistent with the UVS data. In particular, the model lightcurves with λ_c near 152 nm exhibit more acetylene (C_2H_2) opacity than is consistent with the data (these channels encompass the strong first vibrational member of the 3R–X Rydberg transition). At longer wavelengths, the excess opacity in the models is from ethylene (C_2H_4). At shorter wavelengths, where ethane (C_2H_6) is expected to contribute, the model lightcurves are in fairly good accord with the data, except for the egress case at $\lambda_c=148.2$ nm, where the second member of the acetylene 3R–X system makes its appearance. Near the 0.5 mbar level, there is a marked discrepancy with the IRIS-retrieved ethane mixing ratio

Table 3. Reactions, rates and references

	Reaction	Rate expression	References
R1	$^1CH_2+H_2\rightarrow CH_3+H$	$k=9.24\times10^{-11}$	Allen *et al.* (1992); Langford *et al.* (1983); Ashfold *et al.* (1981); Braun *et al.* (1970)
R2	$^1CH_2+CH_4\rightarrow CH_3+CH_3$	$k=6.0\times10^{-11}$	Böhland *et al.* (1985)
R3	$CH+CH_4\rightarrow C_2H_4+H$	$k=5.0\times10^{-11}e^{200/T}$ $k_{max}=1.7\times10^{-10}$	Baulch *et al.* (1992) (see note)
R4	$CH+H_2\xrightarrow{M}CH_3$	$k_o=8.75\times10^{-31}e^{524/T}$ $k_\infty=8.3\times10^{-11}$ $k=\frac{k_\infty k_o M}{k_\infty+k_o M}$	Berman and Lin (1984)
R5	$CH_3+H\xrightarrow{M}CH_4$	$k_o=4.0\times10^{-29}$ $k_\infty=4.7\times10^{-10}$ $k=\frac{k_\infty k_o M}{k_\infty+k_o M}F$	Brouard *et al.* (1989) (see note)
R6	$CH_3+CH_3\xrightarrow{M}C_2H_6$	$k_o=3.5\times10^{-7}T^{-7.03}e^{-1390/T}$ $k_\infty=6.0\times10^{-11}$ $k=\frac{k_\infty k_o M}{k_\infty+k_o M}F$	Baulch *et al.* (1992) (see note)
R7	$H+H\xrightarrow{M}H_2$	$k=2.7\times10^{-31}T^{-0.6}$	Baulch *et al.* (1992) (see note)
R8	$H+C_2H_2\xrightarrow{M}C_2H_3$	$k_o=3.3\times10^{-30}e^{-740/T}$ $k_\infty=1.4\times10^{-11}e^{-1300/T}$ $k=\frac{k_\infty k_o M}{k_\infty+k_o M}F$	Baulch *et al.* (1992) (see note)
R9	$H+C_2H_3\rightarrow C_2H_2+H_2$	$k=5.0\times10^{-11}$	(see R64)
R10	$H_2+C_2H_3\rightarrow C_2H_4+H$	$k=5.01\times10^{-20}T^{2.63}e^{-4298/T}$	Tsang and Hampson (1986); Fahr *et al.* (1995)
R11	$H+C_2H_4\xrightarrow{M}C_2H_5$	$k_o=2.15\times10^{-29}e^{-349/T}$ $k_\infty=4.95\times10^{-11}e^{-1051/T}$ $k=\frac{k_\infty k_o M}{k_\infty+k_o M}$	Lightfoot and Pilling (1987) (see note)
R12	$H+C_2H_5\rightarrow CH_3+CH_3$	$k=7.95\times10^{-11}e^{-127/T}$	Pratt and Wood (1984)
R13	$^3CH_2+H\xrightarrow{M}CH_3$	$k_o=3.1\times10^{-30}e^{457/T}$ $k_\infty=1.5\times10^{-10}$ $k=\frac{k_\infty k_o M}{k_\infty+k_o M}$	Gladstone (1983)
R14	$CH_3+{}^3CH_2\rightarrow C_2H_4+H$	$k=7.0\times10^{-11}$	Tsang and Hampson (1986)
R15	$^3CH_2+C_2H_2\rightarrow$Products	$k=1.99\times10^{-11}e^{-3332/T}$	Böhland *et al.* (1988)
R16	$C_2H+H\xrightarrow{M}C_2H_2$	$k_o=1.26\times10^{-18}T^{-3.1}e^{-721/T}$ $k_\infty=3.0\times10^{-10}$ $k=\frac{k_\infty k_o M}{k_\infty+k_o M}$	Tsang and Hampson (1986)
R17	$C_2H+H_2\rightarrow C_2H_2+H$	$k=1.8\times10^{-11}e^{-1090/T}$	Koshi *et al.* (1992)
R18	$C_2H+CH_4\rightarrow C_2H_2+CH_3$	$k=1.7\times10^{-11}e^{-542/T}$	Opansky (personal communication, 1993)
R19	$C_2H+C_2H_6\rightarrow C_2H_2+C_2H_5$	$k=3.6\times10^{-11}$	Lander *et al.* (1990)
R20	$C_2H+C_2H_2\rightarrow C_4H_2+H$	$k=1.1\times10^{-10}e^{28/T}$	Pederson *et al.* (1993)
R21	p-$C_3H_4+H\rightarrow CH_3+C_2H_2$	$k=9.62\times10^{-12}e^{-1560/T}$	Wagner and Zellner (1972)
R22	$^1CH_2+H_2\rightarrow{}^3CH_2+H_2$	$k=1.26\times10^{-11}$	(see R1)
R23A	$C_2H_3+C_2H_3\rightarrow C_2H_2+C_2H_4$	$k=2.4\times10^{-11}$	Fahr *et al.* (1991)
R23B	$C_2H_3+C_2H_3\xrightarrow{M}C_4H_6$	$k_o=1.3\times10^{-22}$ $k_\infty=1.2\times10^{-10}$ $k=\frac{k_\infty k_o M}{k_\infty+k_o M}$	k_o: Laufer *et al.* (1983) k_∞: Fahr *et al.* (1991)
R24	$C_4H+H_2\rightarrow C_4H_2+H$	$k_{24}=k_{17}$	(see note)
R25	$C_4H+CH_4\rightarrow C_4H_2+CH_3$	$k_{25}=k_{18}$	
R26	$C_4H+C_2H_6\rightarrow C_4H_2+C_2H_5$	$k_{26}=k_{19}$	
R27	$C_4H+H\xrightarrow{M}C_4H_2$	$k_{27}=k_{16}$	
R28	$C_4H+C_2H_2\rightarrow C_6H_2+H$	$k_{28}=k_{20}$	
R29	$C_4H+C_4H_2\rightarrow C_8H_2+H$	$k_{29}=k_{20}$	(see note)
R30	$C_2H+C_4H_2\rightarrow C_6H_2+H$	$k_{30}=k_{20}$	
R31	$C_4H^{**}{}_2+C_4H_2\rightarrow C_8H_2+H_2$	$k=1.5\times10^{-10}$	(see note)
R32	$C_4H_2+H\xrightarrow{M}C_4H_3$	$k_o=1.0\times10^{-26}$ $k_\infty=1.39\times10^{-10}e^{-1184/T}$ $k=\frac{k_\infty k_o M}{k_\infty+k_o M}$	Nava *et al.* (1986) (see note)

Table 3.—*continued*

	Reaction	Rate expression	References
R33	$C_4H_3+H\rightarrow C_4H_2+H_2$	$k=1.2\times10^{-11}$	Yung *et al.* (1984)
R34	$C_4H_3+H\rightarrow C_2H_2+C_2H_2$	$k=3.3\times10^{-11}$	Yung *et al.* (1984)
R35	$C_2+H_2\rightarrow C_2H+H$	$k=1.77\times10^{-10}e^{-1469/T}$	Pitts *et al.* (1982)
R36	$C_2+CH_4\rightarrow C_2H+CH_3$	$k=5.05\times10^{-11}e^{297/T}$	Pitts *et al.* (1982)
R37	$C_2H+C_2H_4\rightarrow C_4H_4+H$	$k=1.3\times10^{-10}$	Lander *et al.* (1990)
R38	$C_2H_5+C_2H_5\rightarrow C_2H_6+C_2H_4$	$k=2.4\times10^{-12}$	Baulch *et al.* (1992)
R39	$^3CH_2+{}^3CH_2\rightarrow C_2H_2+H+H$	$k=3.1\times10^{-10}$	Lovejoy *et al.* (1990)
R40	$^1CH_2+CH_4\rightarrow{}^3CH_2+CH_4$	$k=1.2\times10^{-11}$	(see R2)
R41	$CH_3+C_2H_3\rightarrow CH_4+C_2H_2$	$k=3.4\times10^{-11}$	Fahr *et al.* (1991)
R42	$CH_3+C_2H_5\rightarrow CH_4+C_2H_4$	$k=1.28\times10^{-11}T^{-0.32}$	Tsang and Hampson (1986); Baulch *et al.* (1992) (see note)
R43	$C_2H_5+H\xrightarrow{M}C_2H_6$	$k_0=5.5\times10^{-23}T^{-2}e^{-1040/T}$ $k_\infty=1.5\times10^{-13}e^{-440/T}$ $k=\frac{k_\infty k_0 M}{k_\infty+k_0 M}$	Gladstone (1983)
R44	$CH_4+C_2H_3\rightarrow CH_3+C_2H_4$	$k=2.4\times10^{-24}T^{4.02}e^{-2754/T}$	Tsang and Hampson (1986)
R45	$^3CH_2+H\rightarrow CH+H_2$	$k=4.7\times10^{-10}e^{-370/T}$	Zabarnick *et al.* (1986)
R46	$C_2H_3+C_2H_5\xrightarrow{M}1\text{-}C_4H_8$	$k_0=1.9\times10^{-27}$ $k_\infty=2.5\times10^{-11}$ $k=\frac{k_\infty k_0 M}{k_\infty+k_0 M}$	k_0: Laufer *et al.* (1983) k_∞: Tsang and Hampson (1986)
R47	$C_2H_3+C_2H_5\rightarrow C_2H_4+C_2H_4$	$k=2.81\times10^{-12}$	(see note)
R48	$C_2H_3+C_2H_5\rightarrow C_2H_2+C_2H_6$	$k_{48}=k_{47}$	
R49	$^3CH_2+C_2H_5\rightarrow CH_3+C_2H_4$	$k=3.0\times10^{-11}$	Tsang and Hampson (1986)
R50	$^3CH_2+C_2H_3\rightarrow CH_3+C_2H_2$	$k=3.0\times10^{-11}$	Tsang and Hampson (1986)
R51	$C_2H_5+C_2H_5\xrightarrow{M}C_4H_{10}$	$k_0=6.59\times10^{-6}T^{-6.39}e^{-301/T}$ $k_\infty=1.9\times10^{-11}$ $k=\frac{k_\infty k_0 M}{k_\infty+k_0 M}$	k_0: Laufer *et al.* (1983) (see note) k_∞: Baulch *et al.* (1992)
R52	$CH+C_2H_2\rightarrow C_3H_2+H$	$k=3.5\times10^{-10}e^{61/T}$ $k_{max}=5.3\times10^{-10}$	Baulch *et al.* (1992) (see note)
R53	$CH+C_2H_4\rightarrow p\text{-}C_3H_4+H$	$k=2.2\times10^{-10}e^{173/T}$	Baulch *et al.* (1992)
R54	$CH+C_2H_4\rightarrow a\text{-}C_3H_4+H$	$k_{max}=7.1\times10^{-10}$ $k_{53}=Fk$ $k_{54}=(1-F)k$	(see note)
R55	$CH+C_2H_6\rightarrow$ Products	$k=1.8\times10^{-10}e^{132/T}$ $k_{max}=4.4\times10^{-10}$	Baulch *et al.* (1992) (see note)
R56	$p\text{-}C_3H_4+H\xrightarrow{M}C_3H_5$	$k_0=1.636\times10^{-26}T^{-1.165}$ $k_\infty=6.0\times10^{-11}e^{-1233/T}$ $k=\frac{k_\infty k_0 M}{k_\infty+k_0 M}$	Whytock *et al.* (1976); Wagner and Zellner (1972)
R57	$C_2H_3+C_2H_5\rightarrow CH_3+C_3H_5$	$k=2.5\times10^{-11}-k_{46}$	Tsang and Hampson (1986) (see note)
R58	$CH_3+C_2H_3\rightarrow C_3H_5+H$	$k_0=1.3\times10^{-22}$	k_0: Laufer *et al.* (1983)
R59	$CH_3+C_2H_3\xrightarrow{M}C_3H_6$	$k_\infty=1.2\times10^{-10}$ $k_{59}=\frac{k_\infty k_0 M}{k_\infty+k_0 M}$ $k_{58}=0.002k_\infty$	k_∞: Fahr *et al.* (1991) k_{58}: Tsang and Hampson (1986)
R60	$CH_3+C_2H_5\xrightarrow{M}C_3H_8$	$k_0=1.01\times10^{20}T^{-16.1}e^{-1897/T}$ $k_\infty=3.2\times10^{-10}T^{-0.32}$ $k=\frac{k_\infty k_0 M}{k_\infty+k_0 M}$	k_0: Laufer *et al.* (1983) (see note) k_∞: Tsang (1989)
R61	$CH+H_2\rightarrow{}^3CH_2+H$	$k=2.38\times10^{-10}e^{-1760/T}$	Zabarnick *et al.* (1986)
R62	$H+C_2H_5\rightarrow C_2H_4+H_2$	$k=3.0\times10^{-12}$	Tsang and Hampson (1986)
R63	$CH+H\rightarrow C+H_2$	$k=1.4\times10^{-11}$	Becker *et al.* (1989)
R64	$H+C_2H_3\xrightarrow{M}C_2H_4$	$k_0=1.49\times10^{-27}$ $k_\infty=1.55\times10^{-10}$ $k=\frac{k_\infty k_0 M}{k_\infty+k_0 M}$	Fahr *et al.* (1991); Heinemann *et al.* (1988); Monks *et al.* (1995)

(egress case); the downward transport and loss (via condensation) of ethane in this model is too rapid to maintain the observed abundance. The model agreement with the UVS data at wavelengths 140–145 nm is actually fortuitous, with the overabundance of C_2H_2 and C_2H_4 in the models displayed at longer wavelengths compensating for an under-abundance of C_2H_6. The $f_T(CH_4)$ and resulting $K_{1/2}$ values for the $\lambda_c < 140$ nm channels are listed in Table 4 for the nominal p–T models. The tabulated values differ slightly from the corresponding values for the "*a*" models in Paper 1, owing to the updates in modeling inputs (solar irradiance spectrum, effective solar zenith angles, model atmospheres, etc.) and the fact that reratioing has not been performed.

We subsequently defined K profiles characterized by a small number of layers or zones over which K is held constant, and explored model fits by varying the width and placement of the constant K zones. The upper troposphere, lower stratosphere dynamics modeling of Conrath *et al.* (1991b) suggests a sluggish overturning timescale on the order of 10^9 s, corresponding to an eddy mixing coefficient value of 2×10^3 cm^2 s^{-1}. Photochemical modeling of the IRIS measurements of stratospheric acetylene and ethane emissions (Bézard *et al.*, 1991; Paper 2) also strongly indicates a requirement for a sluggish lower stratosphere if the observed abundances are to be maintained. In view of this, K in the lowermost zone has been constrained to values on the order of 2×10^3 cm^2 s^{-1}, although the extent of this layer has been varied.

We have found that a minimum of three constant K zones are required to give a reasonably good fit to the UVS data, with the maximum K values belonging to the middle layer centered near 10^{-2} mbar beneath the primary photochemical zone (where unit optical depth for Lyman α absorption by CH_4 occurs):

$$\begin{aligned} K &= K_1, && p \geq p_1 \\ &= K_1 \times \left(\frac{p}{p_1}\right)^{\gamma_1}, && p_1 > p \geq p_2 \\ &= K_2, && p_2 > p \geq p_3 \\ &= K_2 \times \left(\frac{p}{p_3}\right)^{\gamma_2}, && p_3 > p \geq p_4 \\ &= K_3, && p \leq p_4 \end{aligned} \qquad (5)$$

where $\gamma_1 = \ln(K_2/K_1)/\ln(p_2/p_1)$ and $\gamma_2 = \ln(K_3/K_2)/\ln(p_4/p_3)$. The placement of the rapid rise in K ($p_1 > p \geq p_2$) is chosen in part to reproduce a ratio of ethane-to-acetylene mixing ratios consistent with the Bézard *et al.* (1991) IRIS analysis and in part to avoid stifling the upward flow of CH_4. Other types of profiles were explored (e.g., the profile form adopted by Yung *et al.* (1984) in their extensive Titan photochemical modeling study), but none were found to lead to fits as successful as models with K profiles defined by the above expression.

The models shown in Fig. 6 illustrate the success (and model limitations) obtained with the form for K represented by equation (5); fitting parameter values for the

---

Notes:
Two body rates are in units of cm^3 molecule^{-1} s^{-1}
Three body rates are in units of cm^6 molecule^{-2} s^{-1}
If f_C and f_n values are presented, then the factor F is given by

$$\log_{10} F = \frac{\log_{10} f_C}{1 + \left[\log_{10}\left(\frac{k_o M}{k_\infty}\right)/f_n\right]^2}$$

where M is the background atmosphere number density

k_3 upper limit is $T = 167$ K rate from Berman and Lin (1983)
k_5 $f_C = 0.902 - 1.03 \times 10^{-3} T$, $f_n = 1$
k_6 $f_C = 0.38e^{-T/73} + 0.62e^{-T/1180}$, $f_n = 0.75 - 1.27 \log_{10} f_C$; bath gas is Ar
k_7 bath gas is H_2
k_8 $f_C = 0.44$, $f_n = 0.75 - 1.27 \log_{10} f_C$; bath gas is He
k_{11} fast rate
$k_{24\text{-}28}$ in lieu of firm evidence, estimating that C_4H rates are the same as their C_2H analogs. See: Kiefer and Von Drasek (1990); Tanzawa and Gardiner (1980); Frank and Just (1980)
$k_{29,30}$ in lieu of firm evidence, estimating that $C_4H + C_4H_2$ and $C_2H + C_4H_2$ have the same rate as R20 (see references for R24–R28)
k_{31} estimating to be kinetic rate limit
k_{32} k_o is an estimate and also a lower limit
k_{42} estimating that $k_{42} = 0.04 \cdot k_\infty$ from R60
$k_{47,48}$ estimating that the disproportionation to recombination ratio is 0.23 (average of C_2H_3 and C_2H_5 self-reactions, 0.3 and 0.15 respectively, from Tsang and Hampson (1986)) and taking $k_{48} = k_{47}$
k_{51} expression from NIST Chemical Kinetics Database V5.0 (Mallard *et al.*, 1993); Laufer *et al.* (1983) presented tabulated data which is reproduced by the NIST expression to 1%
k_{52} upper limit is $T = 171$ K rate from Berman *et al.* (1982)
$k_{53,54}$ upper limit is $T = 160$ K rate from Berman *et al.* (1982); $F = 0.5$
k_{55} upper limit is $T = 162$ K rate from Berman and Lin (1983)
k_{57} estimating that $k_{46} + k_{57} = k_\infty$ from R46
k_{60} expression from NIST Chemical Kinetics Database V5.0 (Mallard *et al.*, 1993); Laufer *et al.* (1983) presented tabulated data which is reproduced by the NIST expression to ~30%

Ingress Case

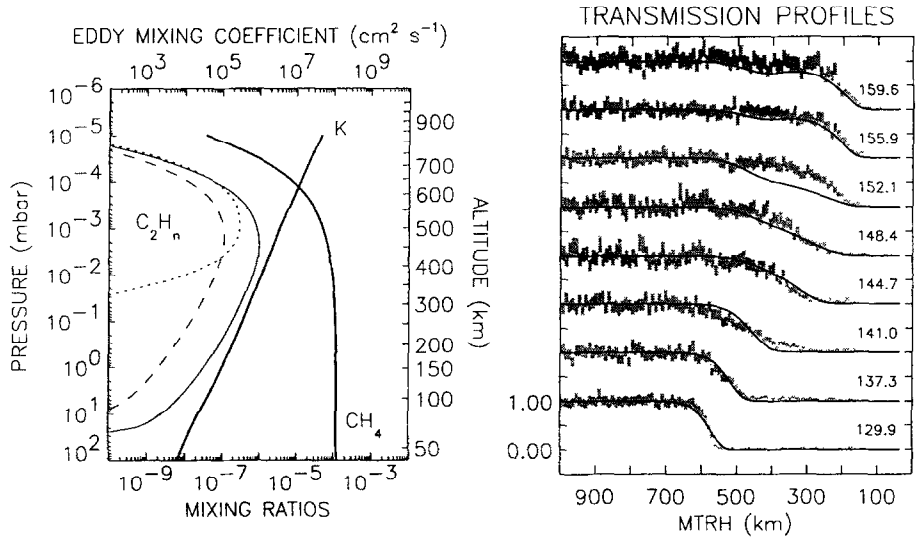

Egress Case

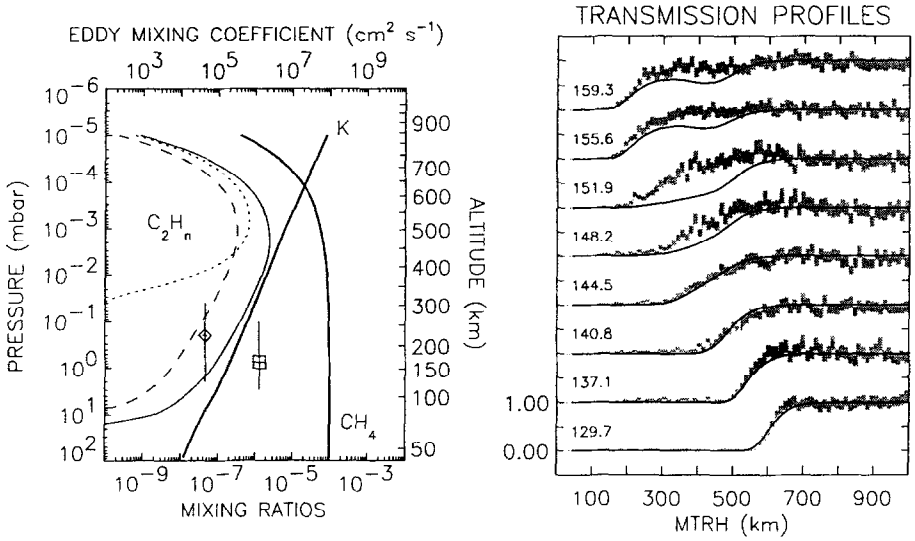

Fig. 5. "Best-fit" photochemical models for K profiles given by equation (4) and corresponding UVS lightcurve comparisons. Hydrocarbon mixing ratio and eddy mixing coefficient profiles are shown in the left-hand panels, transmission profile comparisons in the right-hand panels. Photochemical model profiles: the displayed C_2H_n mixing ratios are C_2H_6 (thin solid curve), C_2H_2 (dash curve), and C_2H_4 (dotted curve); the CH_4 mixing ratio and eddy mixing coefficient (K) profiles are individually labeled (thick solid curves, with the latter referring to the upper abscissa axis). In the egress case (lower panels), IRIS-retrieved C_2H_2 and C_2H_6 abundances are shown (diamond and square symbols, respectively) (Bézard *et al.*, 1991); the vertical bars through these data points indicate the full width at half maximum of the respective contribution functions, while the horizontal crossbars indicate the measurement uncertainties (neglecting temperature dependences). In each case, the respective nominal atmosphere model has been used in the modeling, with altitudes referenced to the respective 1 bar radii. Transmission profile comparisons: the UVS data ranges ($I/I_o \pm \sigma_D$) are gray-shaded and labeled by the channel center wavelengths at 500 km MTRH; the model I/I_o lightcurves are overplotted as solid curves

$\lambda_c < 140$ nm channels are given in Table 4. In the ingress case, models giving good fits for the $\lambda_c < 140$ nm and $\lambda_c > 151$ nm channels consistently failed to provide sufficient opacity at intermediate wavelengths, pointing to either an under-abundance of ethane or the presence of an unmodeled constituent. To gain an idea of the amount of C_2H_6 required to bring about agreement, the ethane mixing ratio profile was scaled by a constant factor; an increase of the model C_2H_6 abundances by a factor of 4.0 brings the model lightcurves into marginal alignment with the UVS data at $\lambda_c = 144.7$ nm and $\lambda_c = 148.4$ nm, but the agreement at $\lambda_c = 152.1$ nm is now worsened. It is

Table 4. Specifications of displayed models

	Case	p–T model	$\lvert\phi^T(H)\rvert$ ($cm^{-2}s^{-1}$)	K profile	$K_{1/2}(\lambda_c < 140\,nm)$ (cm^2s^{-1})	$f_T(CH_4)$	$f(CH_4,z_{1/2})$
INGRESS							
	Fig. 5	nominal [a]	4×10^7	equation (4)	8.1×10^6	12×10^{-5}	2.1×10^{-5}
	Fig. 6	nominal [a]	4×10^7	equation (5)	5.1×10^6	5×10^{-5}	2.4×10^{-5}
	Fig. 8	nominal [a]	4×10^7	stacked K	3.0×10^6	5×10^{-5}	3.1×10^{-5}
EGRESS							
	Fig. 5	nominal [b]	4×10^7	equation (4)	1.7×10^7	10×10^{-5}	2.7×10^{-5}
	Fig. 6	nominal [b]	4×10^7	equation (5)	1.7×10^7	5×10^{-5}	3.1×10^{-5}
	Fig. 7	warm [c]	10^9	equation (5)	4.0×10^6	4×10^{-5}	1.6×10^{-5}
	Fig. 8	nominal [b]	4×10^7	stacked K	6.0×10^6	5×10^{-5}	3.4×10^{-5}

[a] $z_{1/2} = 585\,km$, $p(z_{1/2}) = 2.4\times10^{-4}\,mbar$, $D(CH_4,z_{1/2}) \approx 1.5\times10^6\,cm^2\,s^{-1}$
[b] $z_{1/2} = 608\,km$, $p(z_{1/2}) = 1.8\times10^{-4}\,mbar$, $D(CH_4,z_{1/2}) \approx 2.0\times10^6\,cm^2\,s^{-1}$
[c] $z_{1/2} = 601\,km$, $p(z_{1/2}) = 3.4\times10^{-4}\,mbar$, $D(CH_4,z_{1/2}) \approx 1.1\times10^6\,cm^2\,s^{-1}$

noteworthy, however, that the fit at shorter wavelengths is not compromised. It may be that our adoption of "local" conditions is inappropriate for the ingress data. If the rapid mixing in the middle stratosphere indicated by our models is a manifestation of advection in a meridional circulation system, then the photochemical stability of ethane would suggest that its abundance should be more reflective of global solar illumination conditions.

The egress models are inherently close to such illumination conditions, and generating ethane abundances within the models sufficient to account for the opacities measured by the UVS is not difficult, using the K profile form with three constant layers. In the egress case, however, as in the ingress case, it is difficult to obtain consistent fits across the 140–153 nm interval, since ethane abundances yielding good fits at 140–148 nm result in too much total opacity at 152 nm where the main acetylene spectral signature lies. In Fig. 6 (lower panels) we show a compromise fit geared toward giving agreement with the IRIS-retrieved C_2H_6 mixing ratio at 0.7 mbar while maintaining a marginally acceptable fit to the UVS 152 nm lightcurve. A factor of 3 discrepancy with the IRIS acetylene results is noted.

The middle layer K values displayed in Fig. 6 are representative of the minimum values needed in our modeling explorations to avert excessive C_2H_4 abundances vis-à-vis the UVS data at wavelengths $\lambda_c > 153$ nm. Why is an enhanced K necessary?—briefly, to transport C_2H_4 out of the primary photochemical zone where it is generated by $CH + CH_4 \rightarrow C_2H_4 + H$ (R3 in Table 3) to deeper levels ($p > 10\,\mu bar$) where it is more efficiently consumed in the three body reaction $C_2H_4 + H + M \rightarrow C_2H_5 + M$ (R11). The subsequent fate of C_2H_5 is $C_2H_5 + H \rightarrow CH_3 + CH_3$ (R12), after which methyl radical recombination (R6) can occur. Thus, enhanced K values in the vicinity of the primary photochemical zone (and beneath the nominal homopause) also contribute to ethane production. Even with $K > \approx 10^8\,cm^2\,s^{-1}$ in the middle layer, we have found it necessary to adopt a fast rate for R11, as described in Paper 2. Nevertheless, the inference of the existence of a region of enhanced eddy mixing at pressures beneath the nominal homopause is not critically dependent on the particular reaction rates we have adopted; it is based directly on the strong limits placed on ethylene abundances by the UVS data and on the displacement between C_2H_4 production and loss zones. A more complete description of the pertinent chemistry is given below.

Improved agreement with the UVS lightcurves can be obtained using the "warm" p–T models of Fig. 2 in conjunction with an increase in the downward flux of atomic hydrogen ($\phi^T(H)$) from the thermosphere, as illustrated in Fig. 7. The improvement over the egress case in Fig. 6 is most noticeable at the wavelengths affected by C_2H_2 opacity. Exploratory modeling with $\phi^T(H)$ magnitudes smaller than the adopted nominal value did not affect the photochemical model profiles or data–model comparisons in any notable way. Increasing $\phi^T(H)$, however, acts to reduce both C_2H_2 and C_2H_4 abundances in the primary zone in favor of ethane production and recycling back to CH_4. Use of the warm p–T atmosphere models also aids in improving the model fits to the UVS data, mainly through shifting the pressures sampled by the UVS lightcurves to slightly higher values. Orton *et al.* (1992) (Figure 7 and Table 1) present results illustrating how $f(C_2H_2)$ and $f(C_2H_6)$ values derived from infrared spectral radiance measurements vary with the assumed mean stratospheric temperature on Neptune. Interestingly, increasing the mean temperature from 170 K to 200 K requires a compensating decrease in $f(C_2H_6)$ values of only 10%, while the required decrease in $f(C_2H_2)$ is by a factor of two or more. Adjustment of the IRIS data points in Fig. 7 to the warmer stratospheric temperatures characterizing this model should leave the ethane results in good agreement; however, a discrepancy in C_2H_2 mixing ratios appears to remain similar in magnitude to the discrepancy shown in the Fig. 6 egress case.

To see whether the nominal model fits shown in Fig. 6 could be improved, we have constructed models using piecewise constant K profiles partitioned by scale height above the tropopause (referred to as the "stacked K" case in Table 4). Given the rather large number of free parameters (more than can be uniquely specified by the data), we have simply patterned these K profiles on our previous results and attempted to refine the fits with the data. Typical results are shown in Fig. 8. It has not been possible, with the current set of reactions included in the photochemical model, to improve substantially upon the models based on K profiles of the form given by equation

Ingress Case

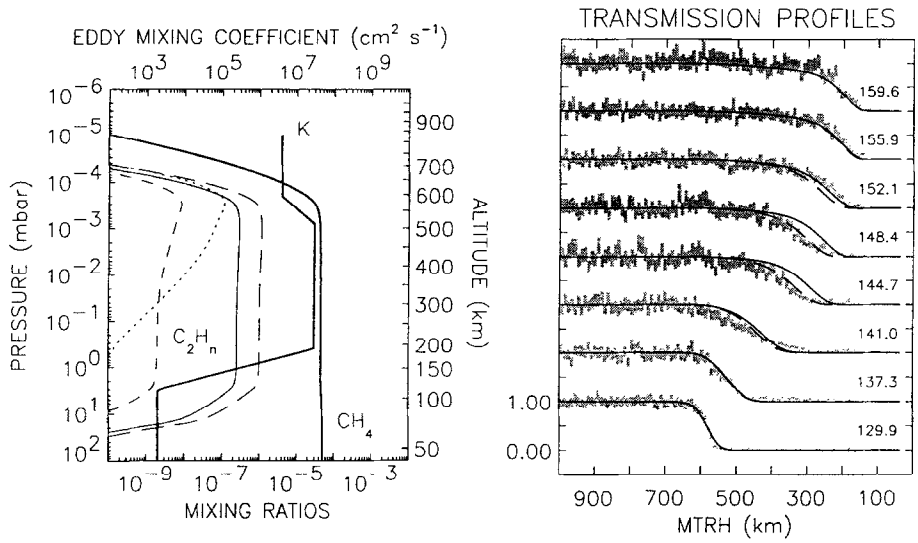

Egress Case

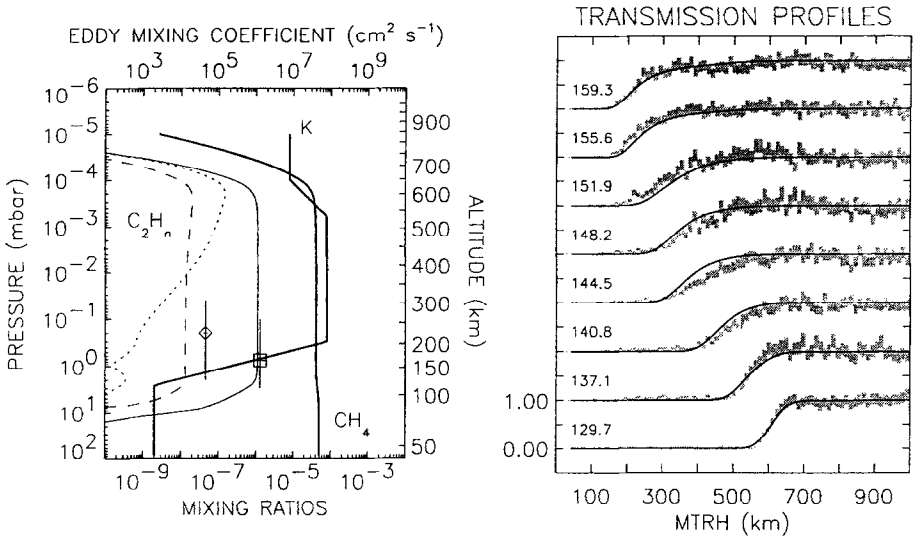

Fig. 6. "Best-fit" photochemical models for K profiles given by equation (5) and corresponding UVS lightcurve comparisons. (See caption to Fig. 5.) In the ingress case, the family of lightcurves obtained by increasing the model-generated ethane mixing ratios uniformly by a factor of 4.0 is also shown (long-dash curves, see text)

(5), suggesting that the use of more sophisticated parameterizations for K are not warranted by the data. The relative under-abundance of ethane is still apparent in the ingress model. The egress model in Fig. 8 is geared toward agreeing with both the IRIS C_2H_6 and C_2H_2 data points while remaining marginally consistent with the UVS data over the 140–153 nm range; the most obvious difficulty is with the UVS 151.9 nm channel, owing to the abundance of acetylene required by the IRIS data.

Column-integrated rates for CH_4 photolysis, net C_2H_2 and C_2H_6 vapor phase production, total hydrocarbon haze mass production (from C_2H_2, C_2H_6, and C_4H_2 condensation), and column-average ratios for CH_4 recycling are given in Table 5 for the models displayed in Figs 5–8. The relevance of column mass production rates of condensible hydrocarbons in the modeling of stratospheric haze distributions on Neptune has been discussed in Paper 2 and is outside the scope of this paper. Recycling of methane following photolysis is a major branch in the chemistry, particularly in the model (shown in Fig. 7) offering our "best fit" to the UVS egress data when the constraints of the IRIS data points are ignored. Net production of ethane is also a significant fraction of CH_4 photolysis in a column sense, but much of the C_2H_6 production actually occurs at pressures >0.1 mbar in the secondary photochemical zone discussed below. A notable difference between the ingress and egress cases is the reduced role of C_2 species photolysis at the longer wavelengths under ingress conditions, resulting in reductions in acetylene abundances larger than exhibited

Egress Case

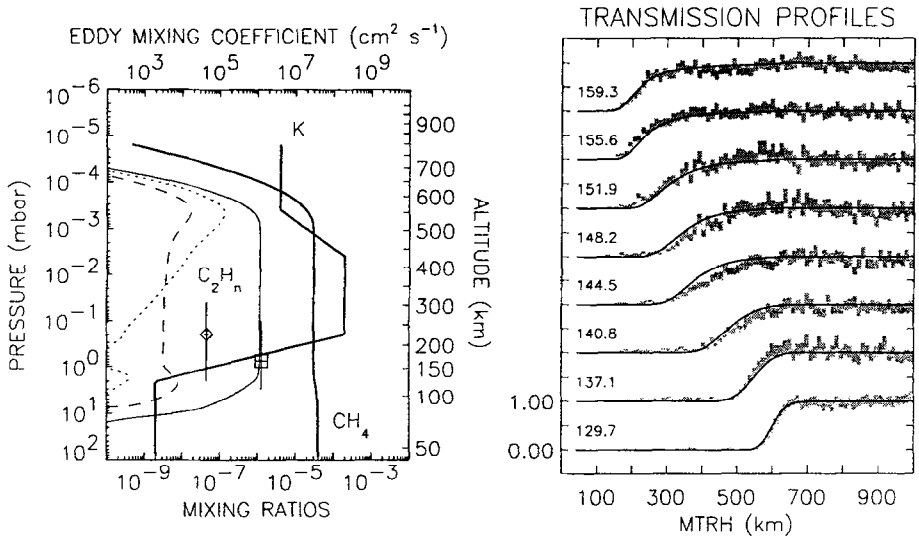

Fig. 7. "Best-fit" egress photochemical model for a K profile given by equation (5) and corresponding UVS lightcurve comparisons, characterized by use of the "warm" egress p–T model (Fig. 2) and an enhanced downward atomic hydrogen flux of $10^9 \text{cm}^{-2}\text{s}^{-1}$ at the top of the modeling region. (See caption to Fig. 5.) Note that the IRIS data points have not been adjusted to compensate for the warmer model temperatures

by ethane and ethylene (which are produced directly from CH_4 photolysis products) when moving from egress to ingress illumination geometries. Results for cases based on the models shown in Fig. 6 but with the LISM Lyman α skyglow "turned off" are also presented in Table 5. The LISM constitutes a minor component to CH_4 photolysis under egress conditions, and its neglect reduces ethane abundances by 30%. Neglecting the LISM in our ingress models severely reduces the photochemical activity; model lightcurves in these cases are dominated almost entirely by H_2 Rayleigh scattering at wavelengths down to 145 nm, with CH_4 photoabsorption dominating at shorter wavelengths. It is actually somewhat surprising how effectively the LISM-driven photolysis of methane in the ingress models shown in Figs 5, 6 and 8 leads to C_2 species abundances comparable to the egress counterparts.

5.1. *Synopsis of C_2-hydrocarbon chemistry*

The photochemistry in the model shown in the lower panels of Fig. 6 (egress case), hereafter treated as our standard model, will be described in more detail. The rates for the main reaction and photodissociation pathways directly determining the mixing ratio distributions of CH_4 and the stable C_2 species are shown in Fig. 9. The corresponding chemical timescales are compared with the eddy mixing and molecular diffusion transport timescales in Fig. 10; the former is given by

$$\tau_K = h_{\text{atm}}^2/K$$

where h_{atm} is the density scale height of the background atmosphere, and the latter by

$$\tau_D = \frac{h_i}{w_D}, \quad w_D = \left| \frac{-D_i}{n_i} \left(\frac{dn_i}{dz} + \frac{n_i}{h_i} \right) \right|$$

where $n_i = Nf_i$, h_i is the diffusive equilibrium density scale height for minor species i, and w_D is the diffusive speed.

Two distinct photochemical zones can be identified. Photolysis of methane by Lyman α (J1 in Table 2) initiates the chemistry in the primary zone at pressures $p \lesssim 3 \times 10^{-2}$ mbar. $^1CH_2$ is for the most part quickly transformed to CH_3 via R1 (see Table 3), with some conversion to $^3CH_2$ via R22. $^3CH_2$ formed from direct methane photodissociation and from $^1CH_2$ de-excitation establishes a condition of near-balance with CH via the reactions R45 and R61 (particularly at pressures $< 10^{-3}$ mbar), but some $^3CH_2$ goes on to form C_2H_4 via R14. Removal of CH is dominated by R3 at pressures $< 10^{-2}$ mbar and by R4 at deeper pressure levels; note that in Fig. 9 R3 is the main route to C_2H_4 in the primary zone and is a minor but significant loss channel for methane. Once CH_3 is formed, production of ethane follows: R6 is the main methyl loss channel at pressures 2×10^{-4}–10^{-1} mbar (R14 and J7 are more important only at lower pressures where mixing ratios are falling off rapidly) and is the only significant ethane production channel at all altitudes. Acetylene is produced mainly via photolysis of ethane (J4a) and ethylene (J3), with $^3CH_2$ recombination (R39) contributing at the highest altitudes. Ethane photolysis also contributes to recycling of methane (J4c) and to ethylene generation (J4b+J4d). While photolysis constitutes the major loss channel for C_2H_4 and C_2H_6, reaction with CH in each case is nonnegligible (R53+R54, and R55, respectively); in the case of C_2H_2, R52 is as important as photolysis.

In brief, the production rates for the major C_2-hydrocarbons outstrip the loss rates in the primary zone except

Ingress Case

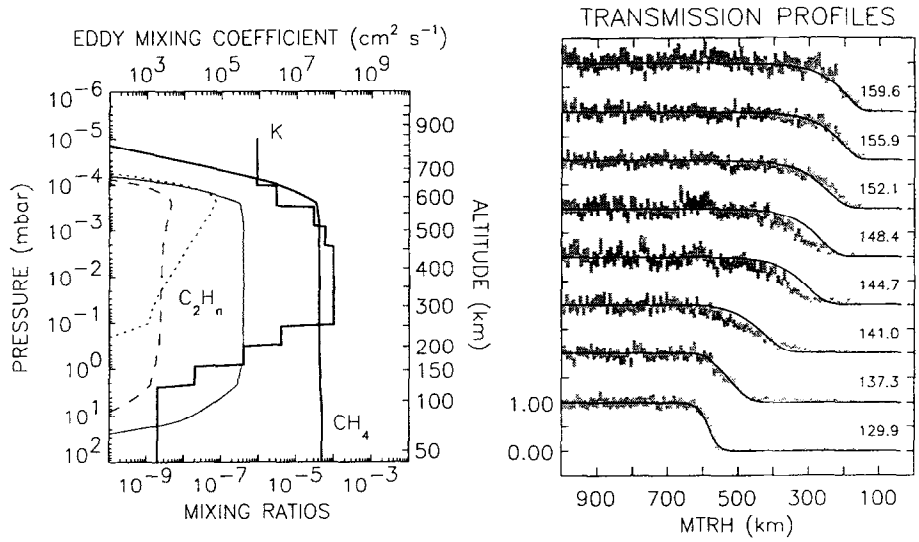

Egress Case

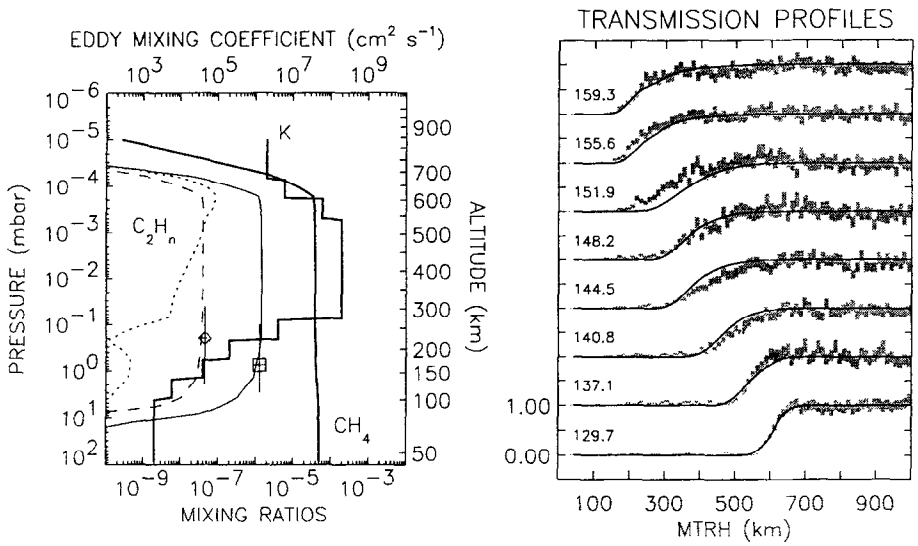

Fig. 8. "Best-fit" ingress and egress photochemical models and corresponding UVS lightcurve comparisons, using models wherein the eddy mixing coefficient is held constant over each scale height displacement above the tropopause ("stacked K" case). (See caption of Fig. 5.)

for ethane at pressures $p < 10^{-4}$ mbar where photolysis is relatively fast (Fig. 10) owing to the lack of shielding by CH_4. Eddy mixing carries these species downward to denser levels where the rates for the 3-body association reactions $C_2H_2+H+M \rightarrow C_2H_3+M$ (R8) and $C_2H_4+H+M \rightarrow C_2H_5+M$ (R11) become relatively efficient; this defines the secondary photochemical zone, centered near $p = 0.5$ mbar. Most of the C_2H_3 recycles to C_2H_2 via R9 but some ends up as ethylene via R64. Most of the C_2H_5 quickly goes on to $C_2H_5+H \rightarrow CH_3+CH_3$ (R12), leading to the production peaks in ethane (R6) and methane (R5) and a net local loss of ethylene, although some recycling occurs (R62). (We can go on to identify a "tertiary" zone, identified by the methane production and loss peaks near 5 mbar, which are initiated by $C_2H_2+h\nu \rightarrow C_2H+H$, C_2+H_2 (J2a,b in Table 2) with the latter followed by $C_2+H_2 \rightarrow C_2H+H$ (R35) and $C_2+CH_4 \rightarrow C_2H+CH_3$ (R36), leading to acetylene recycling (via R17, R18, and R19) and a net conversion of ethane to methane owing to the local release of atomic hydrogen. In terms of the observations, however, this zone has no real significance.)

6. Summary and discussion

The focus in Paper 1 was on the UVS lightcurves expected to be dominated by CH_4 photoabsorption. Although some recycling occurs (via $CH_3+H+M \rightarrow CH_4+M$), the vertical distribution of CH_4 is relatively immune to the photochemistry that follows photolysis, and the main uncer-

Table 5. Column-integrated photochemical rates

	Case	K profile	CH_4 photolysis loss ($cm^{-2}s^{-1}$)	CH_4 recycling	Net production C_2H_2 ($cm^{-2}s^{-1}$)	Net production C_2H_6 ($cm^{-2}s^{-1}$)	Total haze ($g\,cm^{-2}s^{-1}$)
INGRESS							
	Fig. 5	equation (4)	1.1×10^{8}	39%	2.9×10^{6}	4.3×10^{7}	2.3×10^{-15}
	Fig. 6	equation (5)	1.1×10^{8}	46%	3.7×10^{5}	4.1×10^{7}	2.1×10^{-15}
	Fig. 8	stacked K	1.1×10^{8}	45%	2.8×10^{5}	4.1×10^{7}	2.1×10^{-15}
	no LISM	equation (5)	6.9×10^{6}	78%	9.0×10^{4}	1.6×10^{6}	8.3×10^{-17}
EGRESS							
	Fig. 5	equation (4)	4.3×10^{8}	37%	1.4×10^{7}	1.5×10^{8}	8.2×10^{-15}
	Fig. 6	equation (5)	4.2×10^{8}	48%	3.5×10^{6}	1.4×10^{8}	7.1×10^{-15}
	Fig. 7	equation (5)	4.2×10^{8}	64%	2.6×10^{6}	1.0×10^{8}	5.1×10^{-15}
	Fig. 8	stacked K	4.2×10^{8}	42%	6.2×10^{6}	1.4×10^{8}	7.4×10^{-15}
	no LISM	equation (5)	3.3×10^{8}	49%	3.2×10^{6}	1.1×10^{8}	5.4×10^{-15}

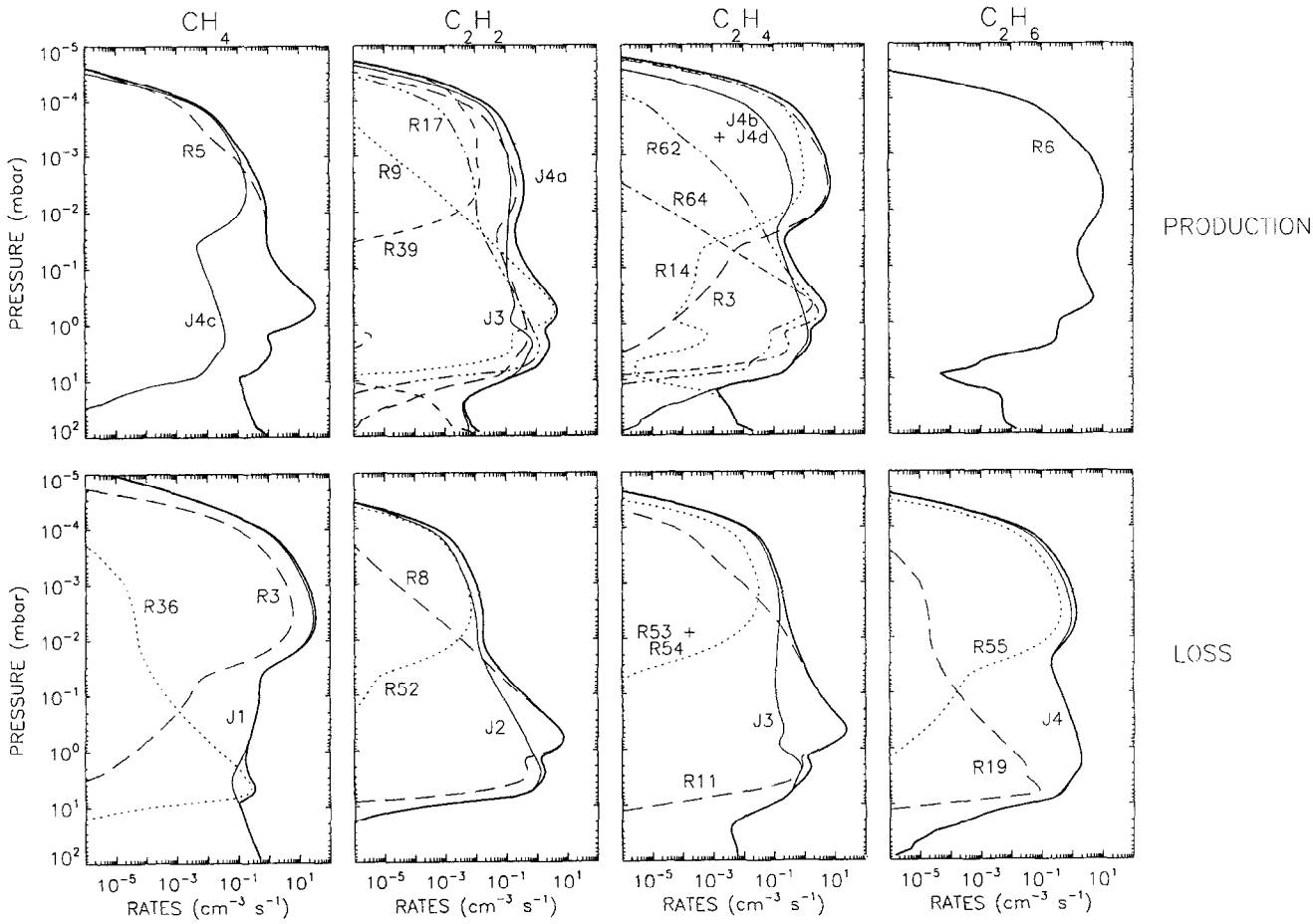

Fig. 9. Photochemical production and loss rates for the major hydrocarbon species, for the egress case of Fig. 6. Both total (thick solid curves) and individual reaction rates are displayed; reaction labels refer to Tables 2 and 3

tainty in the modeling of the UVS 125–140 nm lightcurves lies in the characterization of the background pressure–temperature (p–T) structure. However, at wavelengths longward of 140 nm, CH_4 photoabsorption cross sections fall rapidly and the observed atmospheric opacity in both the ingress and egress UVS data sets stems from other species. As shown in Fig. 1, these lightcurves probe progressively deeper into the atmosphere, to 400 km beneath the half-light altitudes of the 125–140 nm lightcurves. The modeled distributions of the species likely to be responsible for the observed opacity (primarily the C_2 hydrocarbons acetylene (C_2H_2), ethylene (C_2H_4), and ethane (C_2H_6)) depend on model inputs that are not directly observed, especially the strength of vertical eddy mixing

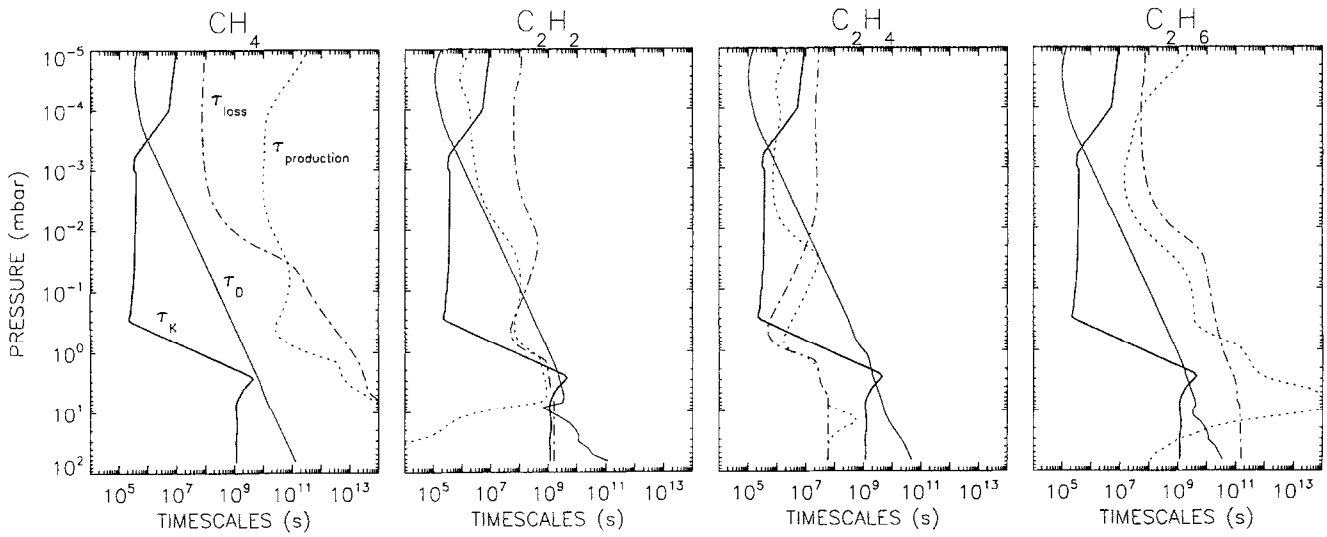

Fig. 10. Timescales for photochemical production (dash curves), photochemical loss (dot-dash curves), transport via molecular diffusion (thin solid curves), and transport via eddy mixing (thick solid curves), for the egress case of Fig. 6

and its variation with altitude. In the current study, photochemical models conforming to the constraints imposed by the 125–140 nm lightcurves and (in the egress case) IRIS measurements (Bézard *et al.*, 1991) have been used in forward modeling simulations of the 140–165 nm UVS lightcurves. A variety of eddy mixing coefficient height profiles have been explored in seeking model fits to the UVS data. The only models exhibiting agreement with the data, shown in Figs 6–8, are those characterized by a vigorously mixed upper stratosphere ($K \approx 10^8$ cm^2 s^{-1} near 10 μbar, decreasing at higher altitudes) overlying a stagnant lower stratosphere. In line with our earlier work, methane mixing ratios in the lower stratosphere on the order of 10^{-4} are required to obtain good agreement between the photochemical models and the UVS lightcurves.

The estimates of $f_T(CH_4)$ derived in our modeling are somewhat at odds with the infrared measurements and analysis of Orton *et al.* (1992), who determined values $7.5^{+18.6}_{-5.6} \times 10^{-4}$ for a mean stratospheric temperature of 168 ± 10 K near 1–10 μbar. Use of the warm model atmospheres (Fig. 2) in our UVS lightcurve simulations permits good fits at the $\lambda_c > 140$ nm channels, as illustrated in Fig. 7, once $f_T(CH_4)$ and $K_{1/2}$ are adjusted (as described in Paper 1) to replicate the correct half-light altitudes. Consequently, a warmer mean stratospheric temperature eases the disagreement, but a sizable discrepancy seems to remain. The analysis of high spatial resolution ground-based imagery data by Baines and Hammel (1994) yielded a nominal value for $f_T(CH_4)$ of 3.5×10^{-4}, between and in marginal agreement with both Orton *et al.* and our modeling results. The independent analysis of the Voyager UVS solar occultation data by Yelle *et al.* (1993), however, led to an inferred $f_T(CH_4)$ range of $0.6–5.0 \times 10^{-3}$, higher even than the Orton *et al.* estimates. As can be seen in all our model fits, we have no difficulty in fitting the UVS lightcurves at wavelengths below 140 nm with $f_T(CH_4)$ values near 10^{-4}. At longer wavelengths, our photochemical models are apparently a little deficient in C_2H_6 compared with the data, and a little overabundant in C_2H_2 in the egress case. The "deficiency" in C_2H_6 in the model lightcurves may actually be due to the neglect of propane in the lightcurve modeling; propane is likely to be a prominent hydrocarbon in the stratosphere of Neptune (Moses *et al.*, 1992) and exhibits a photoabsorption spectrum similar to that of ethane (mean cross section values of a few $\times 10^{-17}$ cm^2 at wavelengths < 145 nm with a rapid fall-off at longer wavelengths). Certainly, the large C_2H_6 abundances invoked by Yelle *et al.* (1993) at pressures < 0.1 mbar are difficult to understand photochemically.

Yelle *et al.* (1993) also attempted to infer the height variation in eddy mixing in Neptune's stratosphere. The values for K derived by Yelle *et al.* from the egress data for 550 km altitude ($K = 2–3 \times 10^6$ cm^2 s^{-1}) are lower than our $K_{1/2}(\lambda_c < 140$ nm) values listed in Table 4. It should be noted, however, that the nominal p–T models used by Yelle *et al.* are warmer than those used in our analysis, which impacts the values for K implied by the UVS lightcurves as discussed in Paper 1. Correcting the Yelle *et al.* values for the difference in assumed mean stratospheric temperature and adjusting to an altitude of 608 km (the nominal egress $z_{1/2}$ altitude) reduce the apparent disagreement considerably. Thus, the values of K(550 km) given by Yelle *et al.* (1993) are roughly in line with our results. There is real disagreement at lower altitudes, however. Yelle *et al.*, using an imposed form for the K profile, claimed that K decreases with decreasing altitude down to $p \approx 0.04$ mbar where our modeling points to maximum K values.

The form of the eddy mixing coefficient profile (given in equation (5)) yielding the most successful model fits to the UVS and IRIS data sets has been discussed in greater detail in Paper 2 (see also Bishop *et al.* (1995)). At both ingress and egress, the placement of the rapid increase in K is roughly consistent with the analysis of probable wave signatures in the RSS occultation data by Hinson and Magalhães (1993). Their analysis relied on the parameterization for wave-driven eddy diffusivity of Lindzen

(1981), despite its limitations (as discussed by Hinson and Magalhães). Interestingly, Lindzen (1981) also argued for a decrease in K as the homopause is approached. However, we are not in a position to explain the large values of K in the middle layer of our models in terms of a particular mixing mechanism; in this work, K is simply a fitting parameter. Nevertheless, it is our belief that, by and large, the chemistry is well accounted for, at least to the extent that our ignorance of dynamical conditions in Neptune's stratosphere introduces greater modeling uncertainties than remaining uncertainties in key reaction rates. Our K profiles yielding good agreement between models and data will hopefully provide useful constraints in dynamical modeling studies. We note in passing that additional constraints on the height profile of eddy mixing in Neptune's stratosphere may be forthcoming from further detailed analysis and modeling of HCN observations at millimeter wavelengths (Lellouch *et al.*, 1994).

Unlike the situation with CH_4, agreement among the various infrared data sets (Kostiuk *et al.*, 1992; Orton *et al.*, 1992; Bishop *et al.*, 1995) and the current photochemical modeling simulations of the egress UVS data shown in Figs 6–8 is reasonably good for C_2H_2 and C_2H_6. A more complete handling of higher order organics, as in the photochemical modeling of Moses *et al.* (1992) and Gladstone *et al.* (1996), may be the key to bringing modeled acetylene and ethane abundances into better joint agreement with available IR and UV data. A severe test will be to see if inclusion of opacity contributions from prominent C_3 species (propane, allene, methylacetylene) will impact the lightcurve modeling while keeping ethylene abundances low enough to remain consistent with the UVS lightcurves at wavelengths longward of 152 nm. Detailed temperature-dependent UV photoabsorption cross sections for these species are currently being measured (R. Wu, personal communication). Once these are available, detailed modeling with an expanded handling of C_3 and C_4 organics will be warranted.

Acknowledgements. We would like to thank Dr. R. Wu for providing us with temperature-dependent C_2H_2 and C_2H_4 photoabsorption cross section data prior to publication, and Lisa DeJong for programming and data modeling assistance. We would also like to thank Dr. B. Sandel and R. Vervack for discussions and data regarding the UVS instrument and occultation measurements. J.B. acknowledges support by NASA under NDAP (grant NAGW-1504). S.K.A. acknowledges support received from NASA's Planetary Atmospheres Program.

References

Akimoto, H., Obi, K. and Tanaka, I. (1965) Primary process in the photolysis of ethane at 1236 Å. *J. Chem. Phys.* **42,** 3864–3868.

Allan, M. (1984) The excited states of 1,3-butadiyne determined by electron energy loss spectroscopy. *J. Chem. Phys.* **80,** 6020–6024.

Allen, M., Yung, Y. L. and Gladstone, G. R. (1992) The relative abundance of ethane to acetylene in the jovian stratosphere. *Icarus* **100,** 527–533.

Ashfold, M. N. R., Fullstone, M. A., Hancock, G. and Ketley, G. W. (1981) Singlet methylene kinetics: Direct measurements of removal rates of $\tilde{a}\,^1A_1$ and $\tilde{b}\,^1B_1$ CH_2 and CD_2. *Chem. Phys.* **55,** 245–257.

Arthur, N. L. (1986) Methyl-radical absorption cross-section at 216.4 nm and rate constant for methyl-radical recombination. *J. Chem. Soc., Faraday Trans.* 2 **82,** 331–336.

Back, R. A. and Griffiths, D. W. L. (1967) Flash photolysis of ethylene. *J. Chem. Phys.* **46,** 4839–4843.

Baines, K. H. and Hammel, H. B. (1994) Clouds, hazes, and the stratospheric methane abundance in Neptune. *Icarus* **109,** 20–39.

Baulch, D. L., Cobos, C. J., Cox, R. A., Esser, C., Frank, P., Just, Th., Kerr, J. A., Pilling, M. J., Troe, J., Walker, R. W. and Warnatz, J. (1992) Evaluated kinetic data for combustion modeling. *J. Phys. Chem. Ref. Data* **21,** 411–734.

Becker, K. H., Engelhardt, B., Wiesen, P. and Bayes, K. D. (1989) Rate constants for $CH(X^2\Pi)$ reactions at low total pressures. *Chem. Phys. Lett.* **154,** 342–348.

Berman, M. R. and Lin, M. C. (1983) Kinetics and mechanisms of the reactions of CH with CH_4, C_2H_6, and n-C_4H_{10}. *Chem. Phys.* **82,** 435–442.

Berman, M. R. and Lin, M. C. (1984) Kinetics and mechanisms of the reactions of CH and CD with H_2 and D_2. *J. Chem. Phys.* **81,** 5743–5752.

Berman, M. R., Fleming, J. W., Harvey, A. B. and Lin, M. C. (1982) Temperature dependence of the reactions of CH radicals with unsaturated hydrocarbons. *Chem. Phys.* **73,** 27–33.

Bézard, B., Romani, P. N., Conrath, B. J. and Maguire, W. C. (1991) Hydrocarbons in Neptune's stratosphere from Voyager infrared observations. *J. Geophys. Res.* **96,** 18961–18975.

Bishop, J., Atreya, S. K., Romani, P. N., Sandel, B. R. and Herbert, F. (1992) Voyager 2 ultraviolet spectrometer solar occultations at Neptune: Constraints on the abundance of methane in the stratosphere. *J. Geophys. Res.* **97,** 11681–11694.

Bishop, J., Atreya, S. K., Romani, P. N., Orton, G. S., Sandel, B. R. and Yelle, R. V. (1995) The middle and upper atmosphere of Neptune. In *Neptune and Triton*, ed. D. P. Cruikshank, pp. 427–487. University of Arizona Press, Tucson, AZ.

Böhland, T., Temps, F. and Wagner, H. Gg. (1985) The contributions of intersystem crossing and reaction in the removal of CH_2 ($\tilde{a}\,^1A_1$) by hydrocarbons studied with the LMR. *Ber. Bunsenges. Phys. Chem.* **89,** 1013–1018.

Böhland, T., Temps, F. and Wagner, H. Gg. (1988) Kinetics of the reactions of CH_2 ($\tilde{X}^3B_1$)-radicals with C_2H_2 and C_4H_2 in the temperature range $296\,K \leq T \leq 700\,K$. *Symp. Int. Combust. Proc.* **21,** 841–850.

Braun, W., Bass, A. M. and Pilling, M. (1970) Flash photolysis of ketene and diazomethane: The production and reaction kinetics of triplet and singlet methylene. *J. Chem. Phys.* **52,** 5131–5143.

Broadfoot, A. L., Atreya, S. K., Bertaux, J. L., Blamont, J. E., Dessler, A. J., Donahue, T. M., Forrester, W. T., Hall, D. T., Herbert, F., Holberg, J. B., Hunten, D. M., Krasnopolsky, V. A., Linick, S., Lunine, J. I., McConnell, J. C., Moos, H. W., Sandel, B. R., Schneider, N. M., Shemansky, D. E., Smith, G. R., Strobel, D. F. and Yelle, R. V. (1989) Ultraviolet spectrometer observations of Neptune and Triton. *Science* **246,** 1459–1466.

Brouard, M., Macpherson, M. T. and Pilling, M. J. (1989) Experimental and RRKM modeling study of the CH_3+H and CH_3+D reactions. *J. Phys. Chem.* **93,** 4047–4059.

Calvert, J. G. and Pitts, J. N. Jr. (1966) *Photochemistry*. Wiley, New York.

Conrath, B. J., Gautier, D., Lindal, G. F., Samuelson, R. E. and Shaffer, W. A. (1991) The helium abundance of Neptune from Voyager measurements. *J. Geophys. Res.* **96,** 18907–18919.

Conrath, B. J., Flasar, F. M. and Gierasch, P. J. (1991) Thermal structure and dynamics of Neptune's atmosphere from Voyager measurements. *J. Geophys. Res.* **96,** 18931–18939.

Conrath, B. J., Gautier, D., Owen, T. C. and Samuelson, R.

E. (1993) Constraints on N_2 in Neptune's atmosphere from Voyager measurements. *Icarus* **101,** 168–172.

Fahr, A., Laufer, A., Klein, R. and Braun, W. (1991) Reaction rate determinations of vinyl radical reactions with vinyl, methyl, and hydrogen atoms. *J. Phys. Chem.* **95,** 3218–3224.

Fahr, A., Monks, P. S., Stief, L. J. and Laufer, A. H. (1995) Experimental determination of the rate constant for the reaction of C_2H_3 with H_2 and implications for the partitioning of hydrocarbons in atmospheres of the outer planets. *Icarus* **116,** 415–422.

Ford, A. L. and Browne, J. C. (1973) Rayleigh and Raman cross sections for the hydrogen molecule. *Atomic Data* **5,** 305–313.

Frank, P. and Just, Th. (1980) High temperature thermal decomposition of acetylene and diacetylene at low relative concentrations. *Combust. Flame* **38,** 231–248.

Gladstone, G. R. (1983) Radiative transfer and photochemistry in the upper atmosphere of Jupiter. Ph.D. Thesis. California Institute of Technology, Pasedena, CA.

Gladstone, G. R., Allen, M. and Yung, Y. L. (1996) Hydrocarbon photochemistry in the upper atmosphere of Jupiter. *Icarus* **119,** 1–52.

Glicker, S. and Okabe, H. (1987) Photochemistry of diacetylene. *J. Phys. Chem.* **91,** 437–440.

Gorden, R. Jr. and Ausloos, P. (1967) Gas-phase photolysis and radiolysis of methane. Formation of hydrogen and ethylene. *J. Chem. Phys.* **46,** 4823–4834.

Hampson, R. F., Jr. and McNesby, J. R. (1965) Vacuum-ultraviolet photolysis of ethane at high temperature. *J. Chem. Phys.* **42,** 2200–2208.

Hara, H. and Tanaka, I. (1973) Photolysis of ethylene at 1634 Å and 1849 Å. *Bull. Chem. Soc. Japan* **46,** 3012–3015.

Heinemann, P., Hofmann-Sievert, R. and Hoyermann, K. (1988) Direct study of the reactions of vinyl radicals with hydrogen and oxygen atoms. *Symp. Int. Combust. Proc.* **21,** 865–873.

Hinson, D. P. and Magalhães, J. A. (1993) Inertio-gravity waves in the atmosphere of Neptune. *Icarus* **105,** 142–161.

Hinteregger, H. E., Fukui, K. and Gilson, B. R. (1981) Observational, reference and model data on solar EUV, from measurements on AE-E. *Geophys. Res. Lett.* **8,** 1147–1150.

Hubbard, W. B., Nicholson, P. D., Lellouch, E., Sicardy, B., Brahic, A., Vilas, F., Bouchet, P., McLaren, R. A., Millis, R. L., Wasserman, L. H., Elias, J. H., Matthews, K., McGill, J. D. and Perrier, C. (1987) Oblateness, radius, and mean stratospheric temperature of Neptune from the 1985 August 20 occultation. *Icarus* **72,** 635–646.

Hunten, D. M. (1975) Vertical transport in atmospheres. In *Atmospheres of Earth and the Planets*, ed. B. M. McCormac, pp. 59–72. Reidel, Norwell.

Kiefer, J. H. and Von Drasek, W. A. (1990) The mechanism of the homogeneous pyrolysis of acetylene. *Int. J. Chem. Kinetics* **22,** 747–786.

Koshi, M., Fukuda, K., Kamiya, K. and Matsui, H. (1992) Temperature dependence of the rate constants for the reactions of C_2H with C_2H_2, H_2, and D_2. *J. Phys. Chem.* **96,** 9839–9843.

Kostiuk, T., Romani, P., Espenak, F. and Bézard, B. (1992) Stratospheric ethane on Neptune: Comparison of ground-based and Voyager IRIS retrievals. *Icarus* **99,** 353–362.

Lander, D. R., Unfried, K. G., Glass, G. P. and Curl, R. F. (1990) Rate constant measurements of C_2H with CH_4, C_2H_6, C_2H_4, D_2, and CO. *J. Phys. Chem.* **94,** 7759–7763.

Langford, A. O., Petek, H. and Moore, C. B. (1983) Collisional removal of CH_2 ($^1A_1$): Absolute rate constants for atomic and molecular collisional partners at 295 K. *J. Chem. Phys.* **78,** 6650–6659.

Laufer, A. H. and McNesby, J. R. (1968) Photolysis of methane at 1236 Å: Quantum yield of hydrogen formation. *J. Chem. Phys.* **49,** 2272–2278.

Laufer, A. H., Gardner, E. P., Kwok, T. L. and Yung, Y. L. (1983) Computations and estimates of rate coefficients for hydrocarbon reactions of interest to the atmospheres of the outer solar system. *Icarus* **56,** 560–567.

Lee, L. C. and Chiang, C. C. (1983) Fluorescence yield from photodissociation of CH_4 at 1060–1420 Å. *J. Chem. Phys.* **78,** 688–691.

Lellouch, E., Romani, P. N. and Rosenqvist, J. (1994) The vertical distribution and origin of HCN in Neptune's atmosphere. *Icarus* **108,** 112–136.

Lias, S. G., Collin, G. J., Rebbert, R. E. and Ausloos, P. (1970) Photolysis of ethane at 11.6–11.8 eV. *J. Chem. Phys.* **52,** 1841–1851.

Lightfoot, P. D. and Pilling, M. J. (1987) Temperature and pressure dependence of the rate constant for the addition of H to C_2H_4. *J. Phys. Chem.* **91,** 3373–3379.

Lindal, G. F. (1992) The atmosphere of Neptune: An analysis of radio occultation data acquired with Voyager 2. *Astron. J.* **103,** 967–982

Lindzen, R. S. (1971) Tides and gravity waves in the upper atmosphere. In *Mesospheric Models and Related Experiments*, ed. G. Fiocco, pp. 122–130. Reidel, Norwell.

Lindzen, R. S. (1981) Turbulence and stress owing to gravity wave and tidal breakdown. *J. Geophys. Res.* **86,** 9707–9714.

Lovejoy, E. R., Alvarez, R. A. and Bradley Moore, C. (1990) The yield of CO in the reaction: $CH_2(\tilde{a}^1A_1) + CH_2CO$. *Chem. Phys. Lett.* **174,** 151–156.

McDonald, J. R., Baronavski, A. P. and Donnelly, V. M. (1978) Multiphoton-vacuum-ultraviolet laser photodissociation of acetylene: Emission from electronically excited fragments. *Chem. Phys.* **33,** 161–170.

McNesby, J. R. and Okabe, H. (1964) Vacuum ultraviolet photochemistry. *Adv. Photochem.* **3,** 157–240.

Mallard, W. G., Westley, F., Herron, J. T., Hampson, R. F. and Frizzell, D. H. (1993) *NIST Chemical Kinetics Database, Version* 5.0. National Institute of Standards and Technology, Gaithersburg, MD.

Monks, P. S., Nesbitt, F. L., Payne, W. A., Scanlon, M., Stief, L. J. and Shallcross, D. E. (1995) Absolute rate constant and product branching ratios for the reaction between H and C_2H_3 at $T = 213$ and 298 K. *J. Phys. Chem.* **99,** 17151–17159.

Mordaunt, D. H., Lambert, I. R., Morley, G. P., Ashfold, M. N. R., Dixon, R. N., Western, C. M., Schnieder, L. and Welge, K. H. (1993) Primary product channels in the photodissociation of methane at 121.6 nm. *J. Chem. Phys.* **98,** 2054–2065.

Moses, J. I., Allen, M. and Yung, Y. L. (1992) Hydrocarbon nucleation and aerosol formation in Neptune's atmosphere. *Icarus* **99,** 318–346.

Mount, G. H. and Moos, H. W. (1978) Photoabsorption cross sections of methane and ethane, 1380–1600 Å, at $T = 295$ K and $T = 200$ K. *Astrophys. J.* **224,** L35–L38.

Mount, G. H., Warden, E. S. and Moos, H. W. (1977) Photoabsorption cross sections of methane from 1400 to 1850 Å. *Astrophys. J.* **214,** L47–L49.

Nakayama, T. and Watanabe, K. (1964) Absorption and photoionization coefficients of acetylene, propyne, and 1-butyne. *J. Chem. Phys.* **40,** 558–561.

Nava, D. F., Mitchell, M. B. and Stief, L. J. (1986) The reaction $H + C_4H_2$: Absolute rate constant measurement and implication for atmospheric modeling of Titan. *J. Geophys. Res.* **91,** 4585–4589.

Okabe, H. (1981) Photochemistry of acetylene at 1470 Å. *J. Chem. Phys.* **75,** 2772–2778.

Okabe, H. (1983) Photochemistry of acetylene at 1849 Å. *J. Chem. Phys.* **78,** 1312–1317.

Orton, G. S., Lacy, J. H., Achtermann, J. M., Parmar, P. and Blass, W. E. (1992) Thermal spectroscopy of Neptune: The stratospheric temperature, hydrocarbon abundances, and isotopic ratios. *Icarus* **100,** 541–555.

Pedersen, J. O. P., Opansky, B. J. and Leone, S. R. (1993) Laboratory studies of low-temperature reactions of C_2H with

C_2H_2 and implications for atmospheric models of Titan. *J. Phys. Chem.* **97,** 6822–6829.
Pitts, W. M., Pasternack, L. and McDonald, J. R. (1982) Temperature dependence of the C_2 ($X\,^1\Sigma_g^+$) reaction with H_2 and CH_4 and C_2 ($X\,^1\Sigma_g^+$ and $a^3\Pi_u$ equilibrated states) with O_2. *Chem. Phys.* **68,** 417–422.
Pratt, G. L. and Wood, S. W. (1984) Kinetics of the reaction of methyl radicals with oxygen. *J. Chem. Soc., Faraday Trans.* 1 **80,** 3419–3427.
Rebbert, R. E. and Ausloos, P. (1972) Photolysis of methane: Quantum yield of $C(^1D)$ and CH. *J. Photochem.* **1,** 171–176.
Romani, P. N. (1996) Recent rate constant and product measurements of the reactions $C_2H_3+H_2$ and C_2H_3+H—Importance for photochemical modeling of hydrocarbons on Jupiter. *Icarus* **122,** 233–241.
Romani, P. N., Bishop, J., Bézard, B. and Atreya, S. (1993) Methane photochemistry on Neptune: Ethane and acetylene mixing ratios and haze production. *Icarus* **106,** 442–463.
Roques, F., Sicardy, B., French, R. G., Hubbard, W. B., Barucci, A., Bouchet, P., Brahic, A., Gehrels, J.-A., Gehrels, T., Grenier, I., Lebertre, T., Lecacheux, J., Maillard, J. P., McLaren, R. A., Perrier, C., Vilas, F. and Waterworth, M. D. (1994) Neptune's upper stratosphere, 1983–1990: Ground-based stellar occultation observations. III. Temperature profiles. *Astron. Astrophys.* **288,** 985–1011.
Sauer, M. C. and Dorfman, L. M. (1961) Molecular detachment processes in the vacuum UV photolysis of gaseous hydrocarbons. I. Ethylene. II. Butane. *J. Chem. Phys.* **35,** 497–502.
Shin, K. S. and Michael, J. V. (1991) Rate constants (296–1700 K) for the reactions $C_2H+C_2H_2\rightarrow C_4H_2+H$ and $C_2D+C_2D_2\rightarrow C_4D_2+D$. *J. Phys. Chem.* **95,** 5864–5869.
Slanger, T. G. and Black, G. (1982) Photodissociative channels at 1216 Å for H_2O, NH_3, and CH_4. *J. Chem. Phys.* **77,** 2432–2437.
Suto, M. and Lee, L. C. (1984) Quantitative photoexcitation and fluorescence studies of C_2H_2 in vacuum ultraviolet. *J. Chem. Phys.* **80,** 4824–4831.
Tanzawa, T. and Gardiner, W. C. Jr. (1980)Reaction mechanism of the homogeneous thermal decomposition of acetylene. *J. Phys. Chem.* **84,** 236–239.
Tsang, W. (1989) Rate constants for the decomposition and formation of simple alkanes over extended temperature and pressure ranges. *Combust. Flame* **78,** 71–86.
Tsang, W. and Hampson, R. F. (1986) Chemical kinetic data base for combustion chemistry. Part I. Methane and related compounds. *J. Phys. Chem. Ref. Data* **15,** 1087–1279.
VanHoosier, M. E., Bartoe, J.-D. F., Brueckner, G. E. and Prinz, D. K. (1988) Absolute solar spectral irradiance 120 nm–400 nm (results from the Solar Ultraviolet Spectral Irradiance Monitor—SUSIM—experiment on board Spacelab 2). *Astron. Lett. Commun.* **27,** 163–168.
Wagner, Von H. Gg. and Zellner, R. (1972) Reaktionen von Wasserstoffatomen mit ungesättigten C_3-kohlenwasserstoffen. II. Die Reaktion von H-atomen mit Methylacetylen. *Ber. Bunsenges. Phys. Chem.* **76,** 518–525.
Whytock, D. A., Payne, W. A. and Stief, L. J. (1976) Rate of the reaction of atomic hydrogen with propyne over an extended pressure and temperature range. *J. Chem. Phys.* **65,** 191–195.
Wu, C. Y. R., Chien, T. S., Liu, G. S., Judge, D. L. and Caldwell, J. J. (1989) Photoabsorption and direct dissociation cross sections of C_2H_2 in the 1530–1930 Å region: A temperature dependent study. *J. Chem. Phys.* **91,** 272–280.
Xia, T. J., Chien, T. S., Wu, C. Y. R. and Judge, D. L. (1991) Photoabsorption and photoionization cross sections of NH_3, PH_3, H_2S, C_2H_2, and C_2H_4 in the VUV region. *J. Quant. Spectrosc. Radiat. Transfer* **45,** 77–91.
Yelle, R. V., Herbert, F., Sandel, B. R., Vervack, R. J., Jr. and Wentzel, T. M. (1993) The distribution of hydrocarbons in Neptune's upper atmosphere. *Icarus* **104,** 38–59.
Yung, Y. L., Allen, M. and Pinto, J. P. (1984) Photochemistry of the atmosphere of Titan: Comparison between model and observations. *Astrophys. J. Supp.* **55,** 465–506.
Zabarnick, S., Fleming, J. W. and Lin, M. C. (1986) Kinetic study of the reaction $CH(X^2\Pi)+H_2\rightleftharpoons CH_2(X^3B_1)+H$ in the temperature range 372 to 675 K. *J. Chem. Phys.* **85,** 4373–4376.

Appendix A

Quantum yields in methane photolysis

The recent work of Mordaunt *et al.* (1993) by itself is incomplete, in that it does not provide sufficient information to unequivocally assign branching ratios (q) at Lyman α for all possible photolysis channels:

$$\begin{aligned} CH_4+h\nu &\xrightarrow{a} {}^3CH_2+H+H \\ &\xrightarrow{b} {}^1CH_2+H_2 \\ &\xrightarrow{c} CH+H_2+H \\ &\xrightarrow{d} CH_3+H \\ &\xrightarrow{e} {}^1CH_2+H+H \end{aligned}$$

Furthermore, no measurements of $^3CH_2$ or $^1CH_2$ quantum yields are available and the data we currently have on CH_3, CH, H_2, and H yields are contradictory. The experimental results on which we rely in our attempt to derive reasonable estimates of the branching ratios at 121.6 nm are:

- net CH_3 yield of 0.5 (Mordaunt *et al.*, 1993).
- net H_2 yield of 0.5 (Laufer and McNesby, 1968). *Note*: the experiment was actually performed at 123.6 nm with a reported quantum yield of 0.58, giving rise to the contradiction that $q_b+q_c=0.58$ but $q_d=0.50$.
- net H yield of 1.0 (Slanger and Black, 1982).
- net CH yield of 0.08 (Rebbert and Ausloos, 1972). *Note*: the measurements were at 123.6 nm (yield = 0.059) and 104.8–106.7 nm (yield = 0.23); the estimate at Lyman α is from simple linear interpolation.

These results, along with the requirement that the branching ratios for channels a–e sum to 1.0, are summarized by the following linear equation:

1	1	1	1	1		q_a		1.00	
0	0	0	1	0		q_b		0.50	CH_3 yield
0	1	1	0	0	×	q_c	=	0.50	H_2 yield
2	0	1	1	2		q_d		1.00	H yield
0	0	1	0	0		q_e		0.08	CH yield

This matrix is singular, owing to the lack of constraints on $^1CH_2$ or $^3CH_2$ yields, with channels a and e each yielding two hydrogen atoms. We choose to neglect channel e, which results in the overdetermined system

1	1	1	1					
0	0	0	1		q_a		CH_3 yield	(0.45 – 0.55)
0	1	1	0	×	q_b	=	H_2 yield	(0.45 – 0.55)
2	0	1	1		q_c		H yield	(≥ 1.0)
0	0	1	0		q_d		CH yield	(0.06 – 0.23)

We solved this system by a least squares method, allowing for

the variations in quantum yields given above, and searched for the "best" solution such that $|1-\sum_i q_i|$ was minimized. It was necessary to renormalize the branching ratios to a sum of 1.0 once the "best" solution had been found: the loss of initial normalization stems from the dropping of one channel and from the "scatter" associated with the least squares solution technique. The result is

q_a	=	0.212		CH_3 yield	0.406
q_b	=	0.282	⇒	H_2 yield	0.382
q_c	=	0.100		H yield	0.930
q_d	=	0.406		CH yield	0.100

To extend these results to other wavelengths, we have adopted the following assumptions and constraints:

- for $\lambda \geq 107$ nm, the branching ratios for the various channels are constant with wavelength (the CH yield is 0.23).
- for longer wavelengths, the CH quantum yield varies linearly with wavelength to reproduce the measured variation, while the CH_3, H_2 & H yields remain independent of wavelength (where energetically allowed).
- $q_a(\lambda > 132) = 0$ and $q_c(\lambda > 133) = 0$.
- photolysis branching ratios sum to 1.0.

The laboratory measurements most needed are (1) the yield of $^3CH_2$ or $^1CH_2$ and (2) the yield of CH, both at Lyman α.